J. Fluid Mech. (1995), *vol.* 285, *pp.* 123–164

Self-similar spiral instabilities in elastic flows between a cone and a plate

By GARETH H. McKINLEY[1] ALPARSLAN ÖZTEKIN,[2] JEFFREY A. BYARS[2] AND ROBERT A. BROWN[2]

[1] Division of Applied Sciences, Harvard University, Cambridge, MA 02138, USA

[2] Department of Chemical Engineering, Massachusetts Institute of Technology, Cambridge, MA 02139, USA

(Received 9 February 1994 and in revised form 19 August 1994)

Experimental observations and linear stability analysis are used to quantitatively describe a purely elastic flow instability in the inertialess motion of a viscoelastic fluid confined between a rotating cone and a stationary circular disk. Beyond a critical value of the dimensionless rotation rate, or Deborah number, the spatially homogeneous azimuthal base flow that is stable in the limit of small Reynolds numbers and small cone angles becomes unstable with respect to non-axisymmetric disturbances in the form of spiral vortices that extend throughout the fluid sample. Digital video-imaging measurements of the spatial and temporal dynamics of the instability in a highly elastic, constant-viscosity fluid show that the resulting secondary flow is composed of logarithmically spaced spiral roll cells that extend across the disk in the self-similar form of a *Bernoulli Spiral.*

Linear stability analyses are reported for the quasi-linear Oldroyd-B constitutive equation and the nonlinear dumbbell model proposed by Chilcott & Rallison. Introduction of a radial coordinate transformation yields an accurate description of the logarithmic spiral instabilities observed experimentally, and substitution into the linearized disturbance equations leads to a separable eigenvalue problem. Experiments and calculations for two different elastic fluids and for a range of cone angles and Deborah numbers are presented to systematically explore the effects of geometric and rheological variations on the spiral instability. Excellent quantitative agreement is obtained between the predicted and measured wavenumber, wave speed and spiral mode of the elastic instability. The Oldroyd-B model correctly predicts the non-axisymmetric form of the spiral instability; however, incorporation of a shear-rate-dependent first normal stress difference via the nonlinear Chilcott–Rallison model is shown to be essential in describing the variation of the stability boundaries with increasing shear rate.

1. Introduction

The torsional motion of a fluid in the narrow gap between a plate and an inverted cone is one of the most common viscometric flows used in the measurement of rheological material functions. A typical cone-and-plate rheometer configuration is shown in figure 1 and consists of a precision machined conical fixture which is mounted with its symmetry axis perpendicular to a flat circular disk. For creeping flow conditions and small cone angles $\theta_0 \ll 1$, the motion between the fixtures is purely azimuthal with no recirculating secondary flow. Measurements of the total torque and normal force exerted by the fluid on the lower plate as a function of the imposed

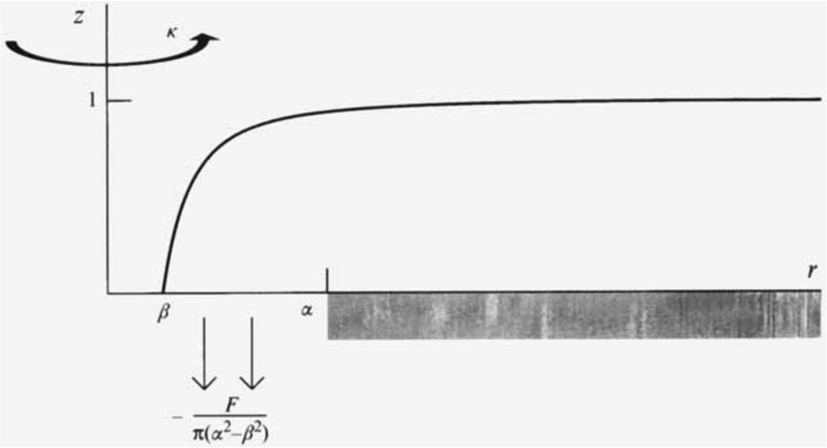

FIGURE 1. Schematic diagram of the cone-and-plate geometry used in experimental measurements.

rotation rate Ω of the cone are used to determine the viscous and elastic material functions of the fluid sample as a function of the deformation rate in the gap. Analysis of the dynamic quantities measured in this geometry is simplified because, in contrast to the corresponding motion between coaxial parallel plates, the circular base flow between the cone and plate is *homogeneous* (at least for slow flows and small cone angles), and the shear rate throughout the fluid is constant with a value given by $\dot{\gamma}_{\theta\phi} \equiv \Omega/\theta_0$ (Bird, Armstrong & Hassager 1987*a*).

For larger cone angles and/or finite Reynolds numbers, it is well known that the purely circumferential flow cannot satisfy the equations of motion and a weak secondary flow consisting of an axisymmetric toroidal vortex develops between the cone and plate (Turian 1972; Heuser & Krause 1979). In Newtonian fluids this secondary motion is driven by centrifugal forces and is directed radially outwards near the surface of the moving fixture. However, early flow visualization experiments by Giesekus (1963) and Walters and coworkers (Walters & Waters 1968; Griffiths & Walters 1970) with polymer solutions in devices with large cone angles ($\theta_0 = 30°, 60°$) showed that elastic hoop stresses directed along the curved streamlines can lead to a steady axisymmetric secondary flow that is *inwardly* directed near the moving fixture.

Such secondary motions in the cone-and-plate geometry have been accurately described analytically by considering perturbation expansions of the governing momentum and constitutive equations in terms of the cone angle θ_0, the Reynolds number $Re \equiv \rho\Omega R^2/\eta$, and, for viscoelastic fluids, in terms of the dimensionless Deborah number $De \equiv \lambda_1 \Omega$ which measures the relative importance of elastic effects to viscous effects in the flow. In these expressions, ρ is the fluid density, η is the fluid viscosity and λ_1 is a characteristic relaxation time for the viscoelastic fluid. Early numerical solutions for a cone-and-plate system of infinite radial extent were obtained by Giesekus (1963) and by Walters & Waters (1968) using second-order fluid models (Bird *et al.* 1987*a*). Very recently, closed-form analytic expressions for the axisymmetric secondary motions of the Oldroyd-B constitutive model have been obtained for both the unbounded case (Olagunju & Cook 1992) and for a finite cone-and-plate geometry incorporating a deformable free surface (Olagunju 1993). These calculations corroborate the flow visualization results described above and also indicate that if both inertial and elastic effects are important in the flow, then two distinct recirculations may develop: an interior, elastically dominated vortex that is inwardly directed near the moving surface and a second, inertially driven recirculation at larger radii that is outwardly directed.

All of the observations and calculations discussed above indicate that for viscous fluids with $Re < 1$ and for small cone angles, $\theta_0 \leqslant 10°$ (0.175 rad), these steady secondary flows have a negligible effect (i.e. less than 1 %) on the experimentally measured material properties of the fluid in a rheometric device. Consequently the flow in a cone-and-plate rheometer is assumed to be steady and one-dimensional at all rotation rates. However, recent analyses have indicated that the presence of elastic normal stresses along the closed circular streamlines can destabilize the torsional motion even under creeping flow and small-gap conditions, and ultimately lead to the onset of more complex non-viscometric motions (Larson 1992). Phan-Thien (1985) considered the stability of the creeping motion between a cone-and-plate for a viscoelastic fluid described by the quasilinear Oldroyd-B model (Bird *et al.* 1987*a*). By considering axisymmetric disturbances that could be represented in a similarity form, Phan-Thien showed that there exists a critical Deborah number $De_{crit} \equiv \lambda_1 \Omega_{crit}$ beyond which the base azimuthal motion is unstable to infinitesimal perturbations. This stability criterion was found to be independent of the cone angle θ_0 and to depend only on the *solvent viscosity ratio* of the fluid defined as $\beta \equiv \eta_s/\eta_0$, where η_s is the viscous contribution of the Newtonian solvent, and η_0 is the total viscosity predicted by the constitutive model. More recent calculations by Olagunju & Cook (1993) extended this analysis for the Oldroyd-B model to include $O(1)$ inertial effects and axisymmetric disturbance kinematics of a more general form. Asymptotic solutions of the governing equations again indicate that at a critical Deborah number, De_{crit}, there is an exchange of stability and loss of uniqueness in the steady solution. Incorporating inertial effects was found to destabilize the steady axisymmetric base solution and to reduce the critical Deborah number below the value found by Phan-Thien.

Experimental measurements also have suggested the presence of viscoelastic flow instabilities in cone-and-plate geometries. Early qualitative flow visualization photographs were presented by Kocherov *et al.* (1973) for polyethylene melts in a disc-type extruder containing a cone-and-plate fixture at the exit. No torque or normal force measurements were presented, but the introduction of tracer particles showed that the fluid pathlines were not concentric circles but of a non-axisymmetric spiral form. The extent of this secondary flow was found to depend on the rotation rate of the conical fixture and on the cone angle θ_0. Although no quantitative measurements were presented, these spiral patterns were labelled by Kocherov *et al.* as 'spirals of Archimedes'. A similar flow instability in cone-and-plate geometries with cone angles $\theta_0 \leqslant 10°$ was reported later by Kulicke & Porter (1979) in rheological studies of shear-thinning polymer solutions. The unstable motion that they observed resulted in a time-dependent increase in the normal force exerted by the fluid on the plates beyond a critical shear rate $\dot{\gamma}_{crit}$ which was found to vary with the molecular weight and concentration of the polymer. No observations of the spatial structure of the flow between the cone and plate were provided; however, the authors did present photographs of the deformable fluid surface at the edge of the conical fixtures. Following the onset of unsteady motion, spatially periodic surface irregularities were observed at the interface which were interpreted in terms of recirculating secondary vortices. These vortices scaled in size with the gap height at the edge of the cone-and-plate rheometer and slowly precessed in the direction of imposed rotation at a rate slower than the rotation rate of the device.

Magda & Larson (1988) performed the first experiments connecting rheological measurements in a cone-and-plate geometry with the linear stability analysis of Phan-

Thien. The experiments utilized highly elastic, constant-viscosity 'Boger fluids' (Boger 1977/78) to eliminate shear-thinning effects, and conical fixtures with angles in the range $2.5° \leqslant \theta_0 \leqslant 10°$. In addition to documenting the time-dependent increase in the torque and normal forces measured in the device, Magda & Larson also demonstrated that the critical shear rate for onset of instability varied inversely with the cone angle and thus corresponded to an approximately constant critical value of the rotation rate, in accord with the analysis of Phan-Thien. Subsequent measurements by Laun & Hingmann (1990) and McKinley *et al.* (1991) corroborated these observations; however, these studies also showed that the detailed dynamics of the elastic cone-and-plate instability that are observed experimentally are not of the form predicted by the Phan-Thien–Olagunju analyses but correspond to a subcritical Hopf bifurcation from the steady base flow.

None of these recent experimental studies in the cone-and-plate device have provided information about the spatial characteristics of the flow instability which can be quantitatively compared with the predictions of stability analyses. In a recent paper (Byars, Öztekin, Brown & McKinley 1994; henceforth referred to as BÖBM) we presented a detailed experimental and theoretical study of the related torsional motion of a viscoelastic fluid between two coaxial parallel disks of radius R separated by a narrow gap $H \ll R$. In this work we showed that the secondary motion that developed between the plates beyond a critical Deborah number, De_{crit}, was not of the axisymmetric von Kármán form, but in fact consisted of Archimedean spiral vortices. These vortices had a radial wavelength that scaled with the gap height, H, and travelled radially outwards across the disk from a critical radial location denoted R^*. The critical onset conditions and spatial form of these disturbances were first modelled by Öztekin & Brown (1993), who considered the linear stability of the Oldroyd-B model to non-axisymmetric spiral disturbances of the form $\exp[\mathrm{i}(\alpha r + m\theta) + \sigma t]$, where α is the radial wavenumber and m is a real integer defining the azimuthal wavenumber. By localizing the resulting linear disturbance equations about a critical radius R^*, it was possible to separate coordinates and obtain a generalized eigenvalue problem that was solved to obtain neutral stability curves for torsional motion between parallel plates. This analysis of the Oldroyd-B model indeed predicted the onset of spiral instabilities at a finite radius and Deborah number, in good qualitative agreement with the available experimental evidence.

The subsequent experiments and computations in BÖBM also showed that a far more complete understanding of these torsional viscoelastic flow instabilities can be obtained by incorporating a nonlinear constitutive model that accurately describes the shear-rate-dependent fluid rheology of the experimental test fluids. In particular, shear thinning in the first normal stress coefficient, $\Psi_1(\dot{\gamma})$, which provides the driving force for the elastic instability, was predicted to restabilize the azimuthal shearing motion between the plates at large radii and confine the spiral vortices to an annular region at intermediate radii across the disks. This localized region of unsteady flow was confirmed by the experimental observations.

No quantitative observations of the azimuthal spatial variation of the secondary flow between a cone and a plate have ever been performed; however, the early work of Kocherov *et al.* (1973) suggests that the unsteady flow observed will not be axisymmetric but also will consist of spiral recirculating vortices. The close similarities between the critical conditions and time-dependent torque/normal-force measurements in cone-and-plate and parallel-plate geometries that have been observed by previous investigators (Magda & Larson 1988; McKinley *et al.* 1991) suggest that the elastic flow instabilities in both configurations may be very similar. There are, however, a number of very important differences between the cone-and-plate and parallel-plate geometries which make our previous analysis for the coaxial-disk geometry inappropriate. Most importantly, in the limit of small cone angles ($\theta_0 \ll 1$) the base shear flow between the cone and plate is a *homogeneous* shear flow with a shear rate, $\dot{\gamma} \equiv \Omega/\theta_0$, that is independent of radial location across the disk. Thus, at any given set of experimental conditions, both the shear rate and the Deborah number will be uniform throughout the fluid, and it is not appropriate to consider localized disturbances about a given critical radius R^*, as was the case for the parallel-plate geometry. In addition, there is no characteristic lengthscale H between the cone and the plate on which to base the scale of the secondary vortices, and we may therefore expect the wavelength of the most unstable, non-local disturbance mode to vary throughout the fluid sample.

These geometric distinctions between the two configurations result in markedly different disturbance kinematics in the cone-and-plate geometry. In this work we present quantitative video-imaging observations of the radial and azimuthal structure of the secondary flow which show that the elastic instability has the spatial form of a *Bernoulli spiral* with a logarithmic radial spacing. Unlike the localized Archimedean spirals observed in our previous parallel-plate studies, this secondary motion extends throughout the fluid, and the wave speed and wavelength of the disturbance increase linearly with the radius. These experiments suggest the definition of a transformed radial coordinate or similarity variable which results in a separable eigenvalue problem when substituted into the linearized momentum disturbance equations. The numerically calculated wavenumbers in the transformed coordinate agree extremely well with the experimental values for a range of cone angles. Even though the shear rate throughout the cone-and-plate device is spatially homogeneous, the dimensionless ratio of the elastic normal stress to viscous shear stress measured in the experimental test fluids varies nonlinearly with the rotation rate and cone angle. We show that it is necessary to incorporate a nonlinear viscoelastic constitutive equation that models this variation in the viscometric properties to even qualitatively describe the experimentally determined stability boundaries in this flow. The connections between these two distinct instabilities in the cone–plate and parallel-plate geometries are also revealed by considering geometries with vanishingly small cone angles.

2. Experimental

2.1. *Geometry*

The geometric configuration of the cone-and-plate device is shown schematically in figure 1, with the origin of a spherical coordinate system $(\hat{r}, \theta, \phi)$ located at the apex of the cone. In this work the lower plate is held fixed while the conical fixture is rotated at a constant angular velocity Ω. A set of conical fixtures with a constant radius of $R = 25$ mm and precisely machined cone angles of $\theta_0 = 4°$, 6°, 10° and 15° were used in the experiments. The lower plate consisted of a smooth, polished Plexiglas sheet carefully aligned to be perpendicular to the axis of rotation. In order to prevent frictional contact between the apex of the cone and the plate, the tip of each cone was truncated to leave a gap of 50 μm at the centre of the device. The conical fixture is rotated by a DC gear-motor (Electrocraft E586) with a tachometer speed control. The rotation rate Ω is used to define a characteristic timescale, and the homogeneous shear rate in the gap is given by $\dot{\gamma} \equiv \Omega/\theta_0$. In these experiments, the maximum rotation rates attained are approximately $\Omega_{max} \sim 10$ rad s^{-1} corresponding to a maximum shear-rate in the 4° cone of $\dot{\gamma}_{max} \sim 150$ s^{-1}.

	0.31% PIB/H100	0.20% PIB/H300
η_0 [Pa s]	13.76	48.1
η_s [Pa s]	8.12	40.1
Ψ_{10} [Pa s^2]	8.96	19.8
λ_1 [s]	0.794	1.24
β	0.59	0.84
L	15	20

TABLE 1. Zero-shear-rate viscometric properties of the two polyisobutylene (PIB) Boger fluids used in the experimental observations of the torsional flow instability. For completeness, the model parameters required for the Oldroyd-B and Chilcott–Rallison constitutive models are also given.

Details of the experimental procedure are discussed in BÖBM and are only briefly summarized here. Fluid samples containing trace quantities of plate-like mica seed particles (Kalliroscope Corp., Groton, MA) are placed between the cone and plate, the fluid sample is illuminated using a fibre-optic light source, and observed from below through the Plexiglas sheet. Images of the fluid motion were recorded using a high-resolution monochrome CCD camera (COHU 4910) and a Super-VHS video recorder (Panasonic AG1960). Individual images (480 × 480 pixels) of the entire cross-sectional area of the disk were digitized from each frame of the videotape using an 8-bit frame-grabber (DIPIX P360), yielding a spatial resolution of ~ 0.10 mm/pixel. Standard digital image processing algorithms are used to correct for non-uniform lighting, remove high-frequency pixel noise, and expand the dynamic range of each image. The time series of resulting digital image intensities $I(\hat{r}, \phi, \hat{t})$ are then used to determine the wave speed, wavelength and spiral structure of the secondary flow as described below in §2.3.

2.2. *Fluid rheology*

Two polyisobutylene (PIB) Boger fluids have been used for the experiments. The first fluid consists of 0.31 wt% high molecular weight PIB (Exxon Vistanex L-120, MW $\sim$ 1.8×10^6 g mol^{-1}), dissolved in 4.83 wt% tetradecane (C14) and 94.86 wt% polybutene (Amoco H100, MW $\sim$ 900 g mol^{-1}), and the second fluid consisted of a lower concentration (0.20 wt%) of the identical polyisobutylene, dissolved in a more viscous solvent consisting of 3.80 wt% C14 and 96.00 wt% of another polybutene grade (Amoco H300, MW $\sim$ 1300 g mol^{-1}). The temperature dependence of the material properties of these two fluids is described by an Arrhenius equation with flow activation energies of $\Delta H = 61.2$ kJ and 62.0 kJ, respectively. The results presented in this paper have all been corrected to a reference temperature of $T_0 = 25$ °C. Detailed rheological data for these fluids have been presented elsewhere (see Quinzani *et al.* 1990 and BÖBM) and are briefly reviewed in table 1.

In table 1, η_0 and Ψ_{10} are the zero-shear-rate values of the viscosity and first normal stress coefficient, respectively, for each polymer solution and η_s is the solvent viscosity. The single relaxation time in the Oldroyd-B model is defined in the zero-shear-rate limit by $\lambda_1 \equiv \Psi_{10}/2(\eta_0 - \eta_s)$, and $\beta \equiv \eta_s/\eta_0$ is the solvent viscosity ratio. Also shown in table 1 is the value of the extensibility parameter L determined from a single-mode fit of the constitutive equation proposed by Chilcott & Rallison (1988) to the steady shear viscometric data. In this constitutive equation, the polymeric contribution to the extra stress $\hat{\boldsymbol{S}}$ is written simply as

$$\hat{\boldsymbol{S}} + \lambda_1(\hat{\boldsymbol{S}}/f)_{(1)} = \eta_p \dot{\gamma}, \tag{1a}$$

where λ_1 is the single time constant in the model, $f \equiv (L^2 + (\lambda_1/\eta_p)\,\mathrm{tr}\,(\hat{\boldsymbol{S}}))/(L^2 - 3)$ is a measure of the nonlinearity in the spring connecting the dumbbells, and η_p is the polymeric contribution to the viscosity. The dimensional shear-rate tensor is given by $\hat{\dot{\gamma}} \equiv \nabla\hat{\boldsymbol{u}} + (\nabla\hat{\boldsymbol{u}})^T$, and the upper-convected derivative for the polymeric extra stress tensor $\hat{\boldsymbol{S}}$ is defined as

$$\hat{\boldsymbol{S}}_{(1)} = \frac{\partial\hat{\boldsymbol{S}}}{\partial\hat{t}} + \hat{\boldsymbol{u}}\cdot\nabla\hat{\boldsymbol{S}} - [(\nabla\hat{\boldsymbol{u}})^T\cdot\hat{\boldsymbol{S}} + \hat{\boldsymbol{S}}\cdot\nabla\hat{\boldsymbol{u}}]. \qquad (1b)$$

The solvent is Newtonian with constitutive equation $\hat{\boldsymbol{\tau}}_s = \eta_s\hat{\dot{\gamma}}$, and the total extra stress tensor resulting from fluid motion is given by the linear superposition, $\hat{\boldsymbol{\tau}} = \hat{\boldsymbol{\tau}}_s + \hat{\boldsymbol{S}}$.

In the limit $L \rightarrow \infty$, the dumbbells become infinitely extensible and (1*a*) simplifies to the upper-convected Maxwell model; the constitutive equation for the total extra stress tensor $\hat{\boldsymbol{\tau}}$ is then equivalent to the Oldroyd-B model (Bird *et al.* 1987*b*). Although the Chilcott–Rallison model was first proposed to describe the finite extensibility of polymer molecules in strong straining motions (cf. Chilcott & Rallison 1988), we have chosen to use it in this study of a torsional shearing motion since it provides a convenient way of systematically varying the elastic properties of a non-Newtonian fluid in the absence of any modifications to the steady shear viscosity. For finite values of L, the model predicts the onset of shear thinning in the first normal stress coefficient beyond dimensionless shear rates of $\lambda_1\dot{\gamma} \cong L^2/[8(L^2-3)]^{1/2}$ with an asymptotic decrease at high shear rates which scales as $\Psi_1(\dot{\gamma}) \sim \dot{\gamma}^{-1}$. As in BÖBM, we then define an 'apparent' relaxation time by $\lambda_1(\dot{\gamma}) \equiv \Psi_1(\dot{\gamma})/2[\eta(\dot{\gamma}) - \eta_s]$ to describe the shear-rate dependence of the elastic properties of the fluid. Henceforth, we explicitly denote a Deborah number based on the zero-shear-rate relaxation time as $De_0 \equiv \lambda_1\Omega$, and a second, shear-rate-dependent quantity as $De(\dot{\gamma}) \equiv \lambda_1(\dot{\gamma})\Omega$, where the apparent relaxation time is evaluated at the shear rate $\dot{\gamma} = \Omega/\theta_0$.

Although the parameter L relates to the extensibility of the polymer molecules and its value would be best determined from extensional viscosity measurements, in the absence of such measurements its value has been chosen to capture the shear-thinning behaviour of $\Psi_1(\dot{\gamma})$ observed experimentally at high shear rates. This criterion yields values of L in the range $12 \leqslant L \leqslant 20$ for both fluids. Very recently, Tirtaatmadja & Sridhar (1993) have reported careful filament stretching measurements on samples of the 0.31 wt% fluid listed in table 1. These measurements suggest that the Trouton ratio of this PIB Boger fluid in an homogeneous uniaxial extensional deformation is in the range $2\text{–}3 \times 10^3$. Using these measurements to determine the extensibility parameter suggests significantly larger values of $L \approx 50$. This important difference in the appropriate value of the model parameter L is discussed further in §5.

2.3. *Coordinate transformation and similarity solution*

The video-imaging measurements presented in §3 show that the spatial form of the secondary flow that develops following onset of the elastic cone-and-plate instability consists of one or more non-axisymmetric recirculating vortices. These roll cells are wound into a well-defined spiral structure with a characteristic logarithmic radial spacing across the disks. In this section we define the normal mode decomposition used to describe infinitesimal perturbations of this form and show that the two-dimensional planform of this representation has the form of self-similar *Bernoulli spiral curves.*

The non-local spatial form of the secondary motion that is observed in the experiments, coupled with the lack of a characteristic lengthscale in the gap between the rotating cone and stationary plate suggests the use of a coordinate transformation to simplify the governing equations. We define a transformed radial coordinate, ξ, by

$$\xi \equiv \ln(\hat{r}/R_0), \qquad (2)$$

where $\hat{r}$ is the dimensional radial coordinate in a $(\hat{r}, \theta, \phi)$ spherical polar coordinate system as shown in figure 1; and R_0 is an arbitrary reference lengthscale, for example the finite radius of the experimental geometry.

When expressed in this dimensionless transformed radial coordinate, the experimental measurements of the separation between adjacent roll cells become equally spaced and the secondary motion can be represented by *Archimedean spirals* as in the previous work by BÖBM for the parallel-plate elastic instability. In transformed coordinates, the disturbances considered for any dimensionless variable f in the linear stability analysis are then represented in the form

$$f(\xi, \theta, \phi, t) = F(\theta)\, \mathrm{e}^{\mathrm{i}\alpha_\xi \xi + \mathrm{i}m\phi + \sigma t}, \tag{3}$$

where α_ξ is the dimensionless wavenumber in the *transformed* radial coordinate, m is an integer indicating the periodicity in the azimuthal direction, σ is the dimensionless complex growth rate of the disturbance scaled with Ω^{-1}, and the complex amplitude function $F(\theta)$ satisfies the boundary conditions of the disturbance equations on the upper and lower fixtures.

In addition to transforming the radial coordinate, it is necessary to scale and nondimensionalize the disturbance velocity components $(\hat{u}_r, \hat{u}_\theta, \hat{u}_\phi)$ that characterize the secondary flow in the equations of motion. Since the secondary motion is driven by the rotation of the conical fixture, by analogy with the von Kármán transformation each component of the disturbance velocity vector is scaled by $(\hat{r}\Omega)$. The analysis here considers only infinitesimal perturbations to the velocity field; for self-consistent calculations of the amplitude of the disturbance velocity field, the continuity equation indicates that the perturbation to the v_θ component of velocity should be $O(\theta_0)$ smaller than the other terms.

As described in §4, introduction of the above transformations for the perturbation velocities and the radial coordinate, forces the linearized momentum and constitutive equations to become independent of $\hat{r}$ and yields a separable eigenvalue problem which can be solved to find the critical Deborah number $De_{crit} = De_{crit}(\alpha_\xi, m, \beta, \theta_0)$ at which $\mathrm{Re}(\sigma) = 0$. In order to perform a quantitative comparison of the video-imaging measurements to the linear stability calculations it is important to understand how the form of the disturbance kinematics given by (2) and (3) is manifested in the experimental apparatus. As in BÖBM, the test fluid is seeded with small plate-like particles which align with the local flow direction. Illumination of the fluid sample and observation of the reflected light, as shown schematically in figure 1, results in a time-series of two-dimensional video images in the $(\hat{r}, \phi)$-plane. If the disturbance kinematics are of the form given by (3) then the intensity I of the images will vary as

$$I(\hat{r}, \phi, t) \sim I_0\, \mathrm{e}^{\mathrm{i}\alpha_\xi \ln(\hat{r}/R_0) + \mathrm{i}m\phi + \sigma t}, \tag{4}$$

where I_0 represents an (unknown) depth average of the reflected light from the fluid sample at each radial position.

Selecting a point in a single video image corresponding to a maximum intensity in the secondary motion and following the location of this recirculating vortex in the $(\hat{r}, \phi)$-plane yields a locus of points given by

$$\mathrm{d}I \equiv \left(\frac{\partial I}{\partial \hat{r}}\right) \mathrm{d}\hat{r} + \left(\frac{\partial I}{\partial \phi}\right) \mathrm{d}\phi = 0 = \frac{\alpha_\xi}{\hat{r}}\, \mathrm{d}\hat{r} + m\, \mathrm{d}\phi. \tag{5}$$

Rearranging and integrating this expression results in a spiral curve $R(\phi)$ defined parametrically by

$$R(\phi) = R_0\, \mathrm{e}^{-(m/\alpha_\xi)\phi}, \tag{6}$$

where $-\infty \leqslant \phi \leqslant \infty$ and R_0 is an integration constant corresponding to the (arbitrary) radial location at which the spiral curve passes through the point $\phi = 0$.

The single curve defined by (5) is known as a *Bernoulli spiral*, and the constant factor $(-\alpha_\xi/m)$ is often defined as a winding number n. Unlike the Archimedean spirals observed by BÖBM, there is no well-defined lengthscale in the radial direction. A rotation of the coordinate system by a factor ϕ_0 is equivalent to a scaling of the radial coordinate by a factor $s \equiv \mathrm{e}^{n\phi_0}$, and this curve is a self-similar or fractal object (Peitgen, Jürgens & Saupe 1993).

Since the azimuthal and transformed radial wavenumbers (m and α_ξ, respectively) are independent parameters, the most general spatial form of secondary motion given by (2) is more complex than a single Bernoulli spiral of the type given in (6); more specifically, the disturbance possesses an additional m-fold degree of azimuthal symmetry. This symmetry is illustrated schematically in figure 2 by plotting the maxima in the disturbance kinematics for a fixed value of the wavenumber α_ξ and different values of the azimuthal wavenumber m. As in BÖBM, non-zero values of the parameter $|m|$ correspond to the integer number of intertwined non-intersecting spiral curves; for $m = 0$ the disturbance corresponds to axisymmetric toroidal vortices with a logarithmic radial spacing.

Both of the wavenumbers (m and α_ξ) describing the disturbance can be determined from experimental measurements of the grey-scale intensity $I(\hat{r}, \phi)$. Measurements of the radial locations (R_i) of successive peak intensities taken radially outwards across the disk at any fixed value of the azimuthal coordinate ϕ are related by a geometric series (cf. (4)):

$$R_{i+1}/R_i = \mathrm{e}^{2\pi/\alpha_\xi}. \tag{7}$$

It is clear from figure 2 that for $m > 1$, the successive peaks R_i and R_{i+1} at a fixed value of ϕ will not correspond to the same recirculating roll cell. Alternatively, following the locus $R(\phi)$ of a single spiral recirculating vortex, describes a path given by (6). Linear regression of ln $R(\phi)$ with the azimuthal coordinate then determines the winding number $-m/\alpha_\xi$ of the spiral. These two measuring techniques are used in §3 to independently determine the wavenumbers α_ξ and m of the elastic cone-and-plate instability.

The wave speed of the disturbance is determined by following the spatial translation of the spiral cells such that $\mathrm{D}I/\mathrm{D}\hat{t} = 0$. The dimensional radial wave speed $\hat{c}_r$ of the cellular disturbance is thus calculated from (4) to vary linearly across the disk as

$$c_\xi \equiv \frac{\hat{c}_r}{\hat{r}\Omega} = -\frac{\mathrm{Im}\,(\sigma)}{\alpha_\xi} \tag{8}$$

and the direction of propagation is determined from the sign of the imaginary part of the eigenvalue σ.

3. Experimental results

Experimental observations are presented that illustrate the procedure by which the spatial and temporal characteristics of the purely elastic cone-and-plate instability are determined. A detailed analysis of the spatial and temporal evolution of the flow instability in the 0.31 wt% Boger fluid for a cone angle of $\theta_0 = 10°$ is presented in §3.1, and the parameters of the spiral that describes the global form of the non-axisymmetric disturbance are determined. The effects on the flow instability of systematically varying the cone angle are demonstrated in §3.2. Finally, the effects of changing fluid rheology are discussed in §3.3.

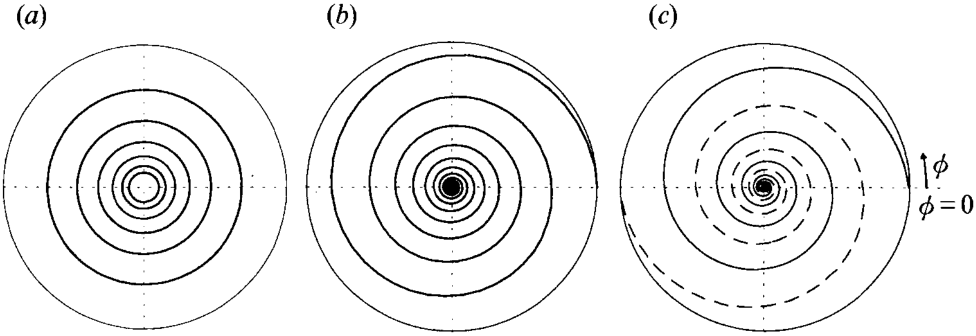

FIGURE 2. Logarithmic spirals of the form given by (3): (*a*) axisymmetric mode, $m = 0$; (*b*) non-axisymmetric mode, $m = 1$; (*c*) nested non-axisymmetric spirals, $m = 2$. The wavenumber α_ξ of the spiral in the transformed radial coordinate is the same in each case.

3.1. *Spiral instability*

The series of grey-scale images shown in figure 3 depict the spatial and temporal evolution of the flow for the 0.31 wt% PIB Boger fluid and a conical fixture with $\theta_0 = 10°$. A steady torsional flow is initially established between the cone and plate at a rotation rate below the critical value Ω_{crit} and this flow is observed for 5 minutes or longer to ensure that it remains stable. Note that even in the steady base flow, the intensity of the light reflected by the seed particles in the fluid is not radially uniform across the disk. This is because the depth of the fluid sample reflecting the incident light increases radially outwards from the apex of the cone which is located at the centre of each image. The Deborah number was then incremented to a supercritical value of $De_0 = 5.28$ by increasing the rotation rate of the conical fixture at the time indicated by 21:00:00 (min:sec:frame) in figure 3. Although the flow is already unstable in figure 3(*a*), the amplitude of the secondary flow is too small to be observed because of the slow temporal growth rate of the disturbance near the critical conditions. Seventy-five seconds later, the secondary flow shown in figure 3(*b*) has grown sufficiently to be observed as a bright spiral vortex. Direct observation of successive frames on the videotape reveal that this spiral vortex slowly translates inwards towards the apex of the cone. The instability continues to grow in intensity, and it is clear from figure 3(*c*) that there is a single spiral that fills the entire region between the cone and plate. Eventually nonlinear interactions become important, as shown in figure 3(*d*), and there is no longer a single clearly defined spatial structure to the flow. However, in contrast to observations of the fine-scale turbulent motion observed following onset of inertial instabilities between a cone and plate (Sdougos, Bussolari & Dewey 1984), it is clear that these elastically driven disturbances continue to propagate throughout the entire fluid sample and are composed of cellular structures with a wide spectrum of spatial wavenumbers. This non-axisymmetric time-dependent flow will persist indefinitely, until either the rotational motion is completely stopped, or the rotation rate is reduced below a second, *lower* critical value for return to the steady two-dimensional torsional flow. This hysteresis is characteristic of a subcritical bifurcation and has been documented clearly in the previous measurements of Magda & Larson (1988) and McKinley *et al.* (1991).

Of course, the complex three-dimensional time-dependent flow that ultimately develops at long times (cf. figure 3*d*) cannot be described by a linearized stability analysis; however, such a linear analysis can describe the initial growth of infinitesimal disturbances in the fluid at short times and the slow transient evolution of the flow

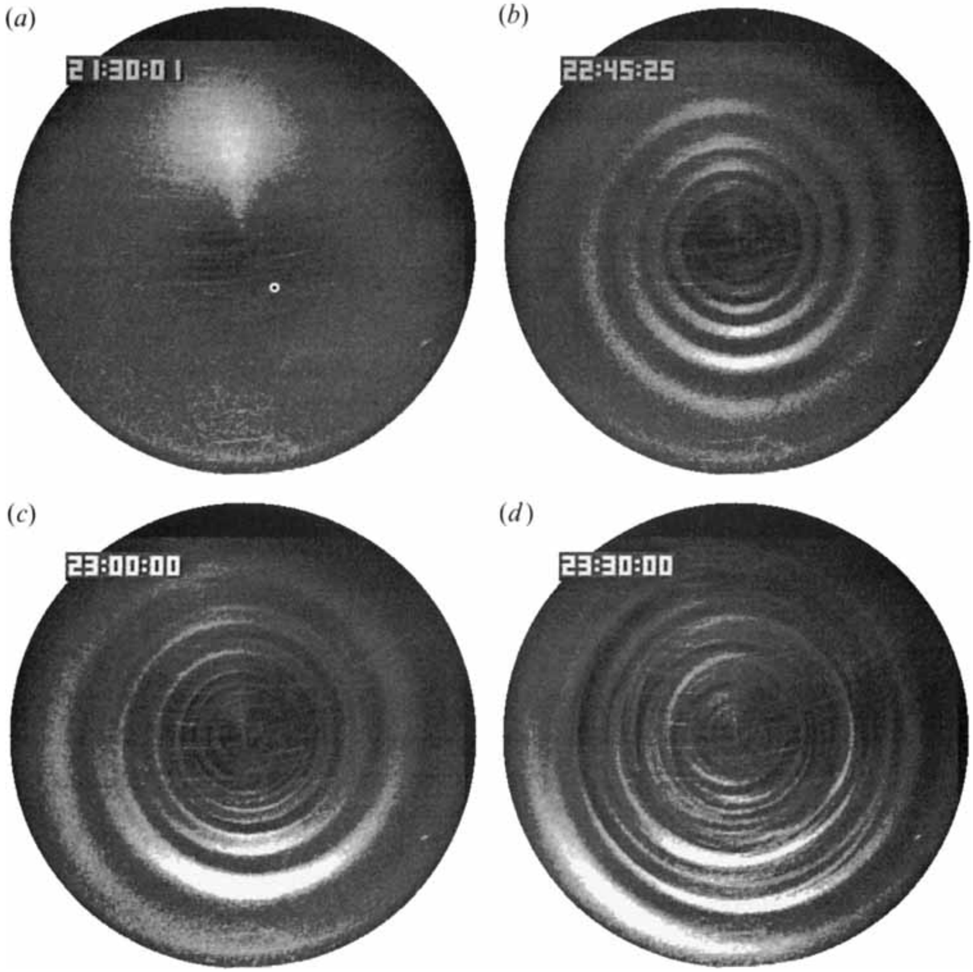

FIGURE 3. Onset and growth of the purely elastic instability observed in the torsional flow of the 0.31 wt% PIB fluid in a cone-and-plate geometry with $\theta_0 = 10°$: (*a*) flow appears stable shortly after the Deborah number is increased to a supercritical value $De_0 = 5.28$ at time $\hat{t} = 21:00:00$ (min:s:frame); (*b*) 75 s later the secondary flow becomes visible; (*c*) inward-travelling non-axisymmetric flow consisting of a single logarithmic spiral vortex; (*d*) ultimate fully nonlinear state. Note that the direction of rotation of the upper conical fixture in this and all subsequent figures is counterclockwise.

away from the steady base motion following a small, carefully controlled increase in the rotation rate beyond the critical value Ω_{crit}.

In order to quantify the structure of the instability, the individual grey-scale images are processed as described in §2 to enhance the visibility of the secondary flow. The time-dependent evolution of the grey-scale intensity along a fixed radial line passing through the origin is shown in figure 4. Each profile is taken from a different video image evenly spaced at 0.2 s (6 video frames) apart and the profiles are offset vertically for clarity. Negative radial coordinates on the abscissa indicate distances along the diametric line given by extending $\phi \rightarrow \phi + \pi$ rad. This series of profiles clearly shows that the recirculation moves slowly inward, and that the instability fills the entire gap, in sharp contrast to the Archimedean spiral instability in the parallel-plate geometry, which only filled an annular region between the disks. We demonstrated in BÖBM that

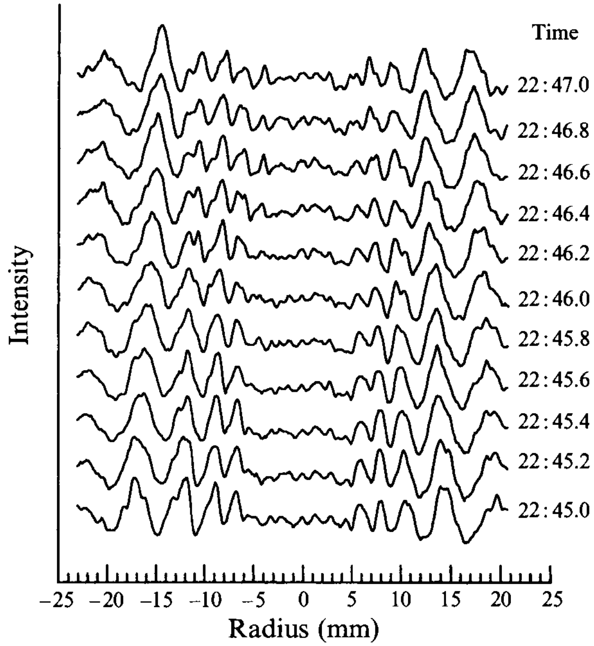

FIGURE 4. Temporal evolution of radial intensity profiles along a fixed line of $\phi = \frac{1}{2}\pi$ rad. The azimuthal origin $\phi = 0$ is indicated in figure 2, and ϕ increases in the counterclockwise direction. The ordinate is vertically offset for each profile to show the translation of the cells, and the timescale is shown in (min:s) to correspond to the images shown in figure 3.

the limited extent of the elastic instability in the parallel-plate geometry results from shear thinning in the normal stresses at the higher shear rates near the outer edge of the disk. By contrast, the homogeneous base flow in the cone-and-plate geometry results in a shear rate that is uniform throughout the sample. The intensity, the distance between successive maxima of the line profiles, and the size of each cell increase with radius, as shown in figure 4. The smaller cell size near the centre of the geometry coupled with the fact that there are fewer seed particles to reflect light in the narrow gap makes it difficult to resolve maxima at radii of less than about $\hat{r} \leqslant 4$ mm (0.16 R).

From the form of the logarithmic similarity transform, we expect the magnitude of the radial component of the wave speed, $\hat{c}_r$, to increase linearly with radius (cf. (8)). Although the profiles of figure 4 clearly show that the spiral travels radially inwards, it is difficult to quantitatively measure $\hat{c}_r$ from these profiles. The radial position of each maximum can be found at each time step, but any estimates of the wave speed require assuming that $\hat{c}_r$ is constant over some interval $\Delta\hat{t}$. A more direct approach is to calculate the wave speed in transformed coordinates (ξ, θ, ϕ), since the dimensionless wave speed c_ξ is constant. The displacement of the ξ-location of each peak with dimensionless time t is shown in figure 5. From such plots, the dimensionless wave speed of the elastic spiral instability in a 10° cone-and-plate geometry was calculated to be $c_\xi = -0.0107 \pm 0.0030$.

A sequence of radial profiles similar to those in figure 4 were also obtained at different angular positions, at a fixed time, in order to study the azimuthal structure of the instability. The wavenumber of the spiral varies linearly with radial position in physical $(\hat{r}, \theta, \phi)$-space, but is a constant in the transformed (ξ, θ, ϕ)-coordinates. Without any additional knowledge of the spatial structure of the flow, α_ξ is determined from the geometric series of the radial locations of successive peaks using (7). The plot

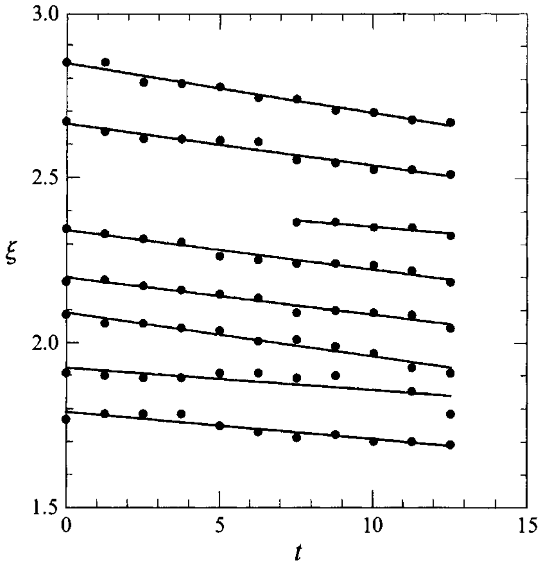

FIGURE 5. Positions of the peaks measured from the intensity profiles of figure 4 for $De_0 = 5.28$, $\theta_0 = 10°$ in the transformed domain (ξ, θ, ϕ) as a function of dimensionless time. The wave speed is calculated to be $c_\xi = -0.0107 \pm 0.0030$.

of the dimensionless ratio R_{i+1}/R_i shown in figure 6(*a*) gives an average value of $R_{i+1}/R_i = 1.345$, corresponding to a dimensionless wavenumber of $\alpha_\xi = 21.2$. The value of m describing the non-axisymmetric structure of the flow instability often can be determined in experiments directly by inspection of images such as figure 3, but for higher mode numbers a more robust regression technique is necessary. In the (ξ, θ, ϕ)-domain the spiral is of Archimedean form, so a linear regression of the experimental data analogous to those reported in BÖBM yields the best fit values of α_ξ and ϕ_0 for a given choice of m. Selection of the Archimedean spiral which most closely describes the overall spatial form of the secondary motion is based on the linear regression which results in the highest correlation coefficient. For the elastic instability shown in figures 3–5 we find that $m = -1$, where modes $m < 0$ indicate 'negative angle spirals' which spiral radially *outwards* as ϕ increases (cf. (6)). The ability of this spiral form to accurately describe the experimental data is demonstrated in figure 6(*b*), where regression of the (ξ, ϕ)-coordinates of each peak R_i to (6) yields a single curve. For $|m| > 1$, there would be $|m|$ different curves corresponding to $|m|$ intertwined spiral vortices each offset by an angular displacement of $2\pi/m$. The slope of this single line gives the winding number n of the spiral defined in (6) as $n = 0.047$, in good agreement with the values of m and α_ξ independently determined above.

The data in figure 6(*b*) can be viewed as the spiral structure of the elastic cone-and-plate instability in (ξ, θ, ϕ)-coordinates when 'unwrapped' in the ϕ-direction. This description is contrasted directly to the original video-imaging observations in figure 7, where the best-fit line from figure 6(*b*) has been transformed back in $(\hat{r}, \theta, \phi)$-coordinates and juxtaposed directly with a raw image of the secondary flow structure. It is clear that a single Bernoulli spiral provides an excellent description of the elastic cone-and-plate instability.

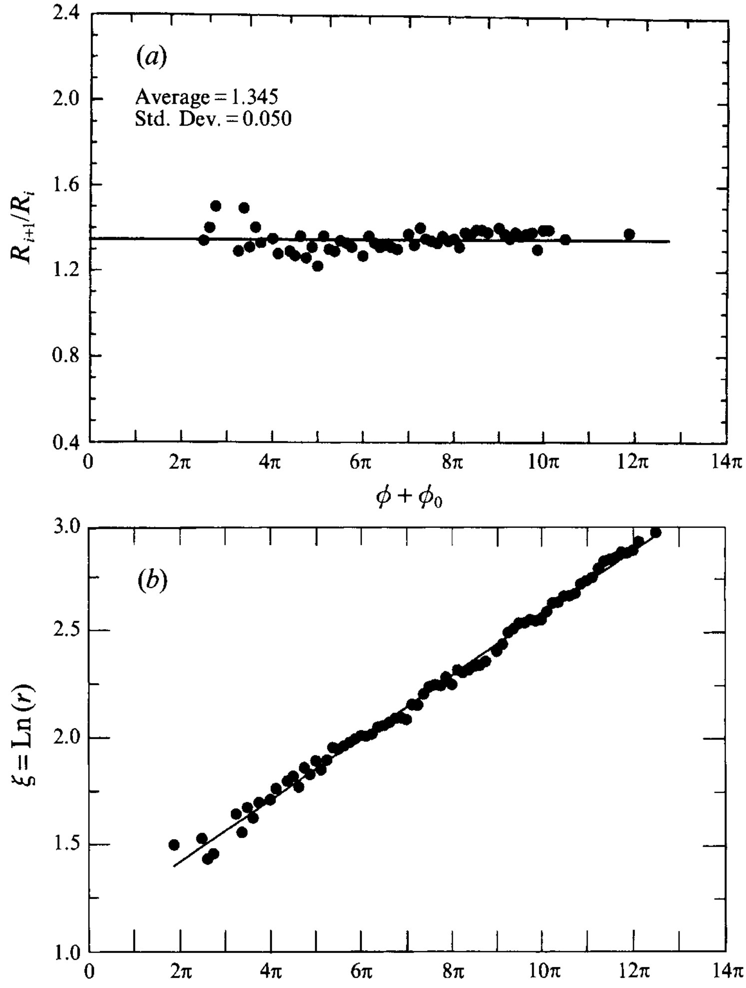

FIGURE 6. Determination of the spatial structure of the secondary flow, $De_0 = 5.28$, $\theta_0 = 10°$. (*a*) Ratio of the values of the radial positions of successive peaks (R_i, R_{i+1}). The wavenumber is calculated as $\alpha_\xi = 21.2$. (*b*) ξ-positions of the peaks as a function of azimuthal position lie on a single curve with $n = 0.047$ ($R^2 = 0.9945$).

3.2. *Variation with cone angle* θ_0

Similar experimental measurements to those described above have also been conducted with the 0.31 wt % PIB Boger fluid using conical fixtures with cone angles of 4°, 6° and 15°. In the interests of brevity we only summarize the key features of the elastic instability in each geometry. Quantitative comparisons of the experimental data with linear stability calculations are presented in §§5 and 6. In general, the observations show that as the cone angle is increased, the critical Deborah number De_{0crit} increases and the transformed radial wavenumber α_ξ of the disturbance decreases. In addition to this trend, the azimuthal mode number of the most unstable non-axisymmetric disturbance is also found to increase as the cone angle decreases. In the 6° cone-and-plate geometry a logarithmic spiral instability with $m = -3$ is observed very close to the critical onset conditions. The three intertwined branches of this spiral instability are shown in figure 8 next to an image of the flow at $De_0 = 4.95$. The wavenumber in this

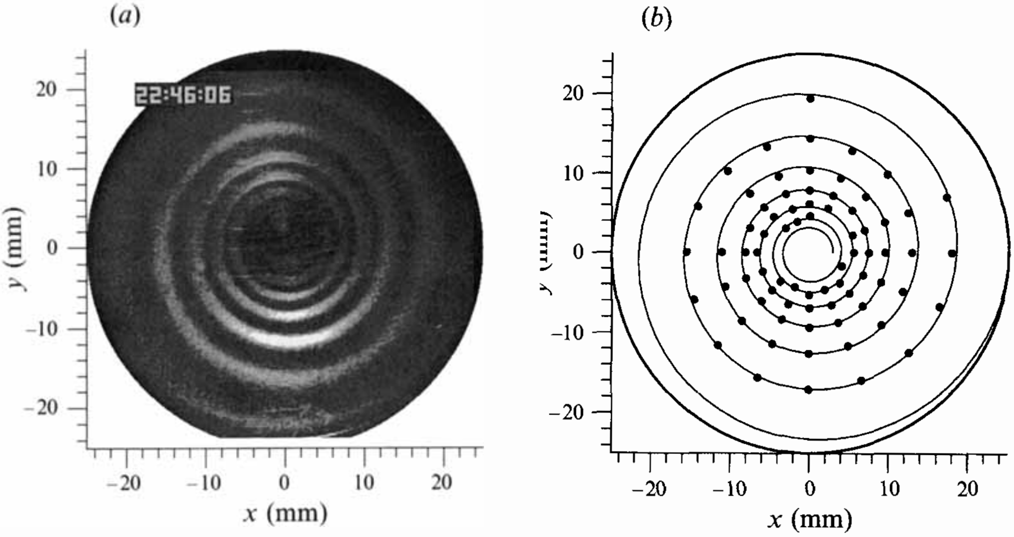

FIGURE 7. (*a*) Raw video image of the flow instability observed at $De_0 = 5.28$ and $\theta_0 = 10°$; (*b*) locations of peaks obtained from processed image and the best fit of (6) to these positions with $m = -1$, $\alpha_\xi = 21.2$ and $\phi_0 = -1.12$ rad.

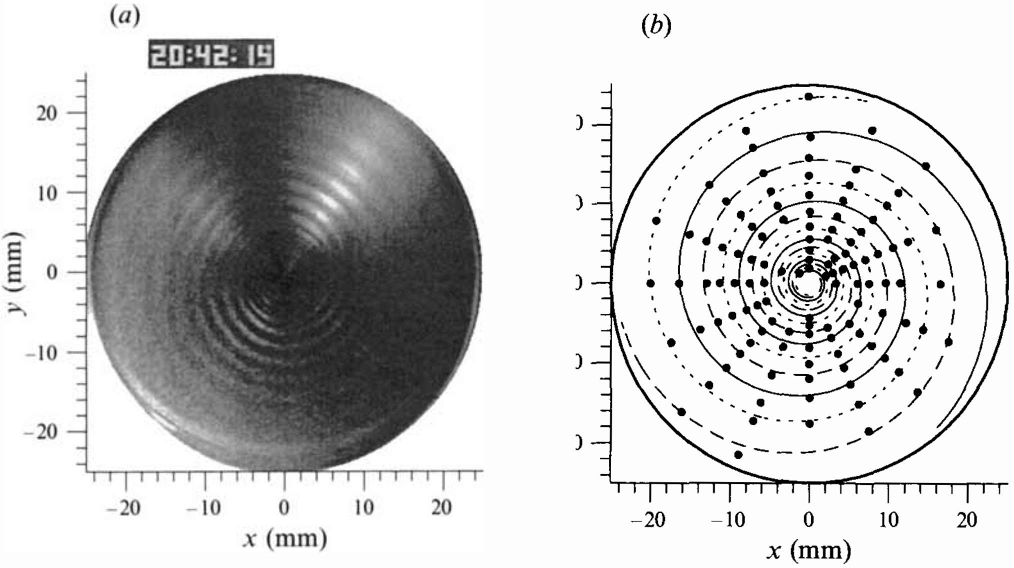

FIGURE 8. (*a*) Raw image of the flow instability at flow conditions of $De_0 = 4.95$ in the 6° cone-and-plate geometry. (*b*) Locations of peaks obtained from processed image (●) and the best fit of (6) to these positions with $m = -3$, $\alpha_\xi = 30.4$ and $\phi_0 = -0.25$ rad.

geometry is determined to increase to $\alpha_\xi = 30.4$ and the dimensionless wave speed decreases slightly from the value determined in the 10° geometry to $c_\xi = -0.0128$. This increase in the azimuthal wavenumber at lower cone angles is consistent with our linear stability calculations discussed in §5.

For the largest conical fixture ($\theta_0 = 15°$), gravitational body forces overcame the surface tension in the large gap at the outer edge of the cone, and observations of the static fluid meniscus shape showed that fluid only bridged the region between the fixtures out to a reduced radius of $R \sim 13$ mm. For this large cone angle, the base flow

Fluid	θ_0 (deg.)	De_0	α_ξ	c_ξ	m
0.31% PIB ($\beta = 0.59$)	4	—	—	—	—
	6	4.95	30.3	−0.0128	−3
	10	5.28	21.2	−0.0107	−1
	15	6.32	16.0	−0.0009	−1
0.20% PIB ($\beta = 0.84$)	4	—	—	—	—
	6	7.60	45.0	−0.0001	0
	10	5.87	16.6	−0.0147	−1

TABLE 2. Summary of the variations in the Deborah number, wavenumber, wave speed and azimuthal mode number at onset of the elastic instability observed experimentally in two elastic Boger fluids over a range of cone angles.

is not expected to be purely azimuthal (Walters & Waters 1968; Olagunju 1993); however, no radial recirculation was discernible from flow visualization. Despite these experimental non-idealities, as the Deborah number is incremented to a critical value of $De_0 = 6.32$, a negative angle spiral instability with $m = -1$ is still observed in the fluid sample. The wavenumber is determined to be $\alpha_\xi \approx 16.0$ and the wave speed is reduced to a value of $c_\xi = -9.0 \times 10^{-4}$.

These variations in the critical conditions for onset of the instability with cone angle are not unexpected and can be at least qualitatively explained by a stability analysis for the quasilinear Oldroyd-B constitutive model. However, the most striking observation is that for a cone angle of 4°, no elastic instability was observed at any rotation rate up to the maximum obtainable Deborah number of $De_0 = 8.31$ ($Re = 0.42$). The possibility that this apparent lack of instability resulted simply from insufficient seeding in the thin fluid sample to reveal the secondary motion was eliminated by performing careful supplementary experiments in a conventional rheometer (Rheometrics RMS-800). No time-dependent variations in either the total torque or the normal force exerted on the fixtures was detected over the same range of De_0. As we discuss in §5.2, the complete elimination of this elastic instability cannot be explained using the quasilinear Oldroyd-B model, which actually predicts that the critical Deborah number should *decrease* monotonically as the cone angle decreases. However, the restabilization of the base flow is explained by incorporating a constitutive equation that predicts a shear-rate-dependent first normal stress coefficient into the analysis. By decreasing the cone angle of the geometry, the shear rate $\dot{\gamma} = \Omega/\theta_0$ experienced by the fluid sample is increased at any value of the rotation rate. Since the apparent relaxation time $\lambda_1(\dot{\gamma})$ of the test fluids decreases with increasing shear rate, we show in §5.3 that the increasing relative importance of viscous effects for small cone angles will ultimately restabilize the base viscometric motion at all rotation rates.

3.3. *Effect of fluid rheology*

In order to explore the sensitivity of the spiral instability to small modifications in the fluid rheology, tests were also conducted in each conical fixture with samples of the 0.20 wt% PIB/PB-H300/C14 Boger fluid. For completeness, the wavenumbers and wave speeds for each of the experimental conditions explored in this work are shown in table 2.

In the 0.20 wt% elastic fluid, spiral instabilities only could be observed for the 6° and 10° cones. In the 10° cone a single inward-travelling spiral ($m = -1$) was again observed, with a wavenumber slightly lower than that calculated in the 0.31 wt% fluid.

However, for the 6° cone the instability had the form of nearly stationary axisymmetric cells, which were poorly defined and hard to resolve with the imaging system. Although it is dangerous to infer trends from only two data points, the progressive increase in the dimensionless wavenumber α_ξ of the spiral instability for the 0.20 wt% fluid appears similar to that discussed in detail above for the 0.31 wt% fluid. Increasing the solvent viscosity ratio also appears to consistently shift the elastic instability to higher Deborah numbers, as we have discussed previously in BÖBM.

We show below in §§4 and 5 that most of these variations in the spatio-temporal characteristics of the instability can be explained by linear stability analysis of the Oldroyd-B model. Somewhat more puzzling for the 0.20 wt% fluid data shown in table 2 is the apparent reversal in the trend of progressively decreasing values of the critical Deborah number with smaller cone angles. In §§5.3 and 5.4 we show that this trend can be explained, at least qualitatively, by considering the stability of a nonlinear constitutive model.

4. Linear stability analysis

4.1. *Governing equations and base solution*

The linear stability analysis is based on the creeping torsional motion of a viscoelastic fluid contained between a cone and a flat circular plate, as shown in figure 1. In the current work, the bottom plate is held stationary and the conical fixture with included angle $(\pi-2\theta_0)$ is rotated about its vertical axis with a constant angular velocity Ω. The kinematics are described in a spherical coordinate system $(\hat{r},\theta,\phi)$ with the origin located at the apex of the cone. Throughout the following development, dimensional variables are denoted explicitly by a caret. The inertialess governing equations for mass and momentum conservation in dimensional form are

$$\nabla\cdot\hat{\boldsymbol{u}}=0 \tag{9}$$

and

$$\nabla\cdot\hat{\boldsymbol{\tau}}-\nabla\hat{p}=\boldsymbol{0}. \tag{10}$$

Here $\hat{\boldsymbol{u}}$ is the velocity vector and the total extra stress is decomposed as $\hat{\boldsymbol{\tau}}\equiv\hat{\boldsymbol{S}}+\eta_s\hat{\dot{\boldsymbol{\gamma}}}$, where $\hat{\boldsymbol{S}}$ is the polymeric contribution to the extra stress and is given by the Chilcott–Rallison constitutive model defined by (1).

The boundary conditions on the velocity field $\hat{\boldsymbol{u}}$ are

$$\hat{\boldsymbol{u}}^T(\hat{r},\tfrac{1}{2}\pi-\theta_0,\phi,\hat{t})=(0,0,\hat{r}\Omega\sin\theta),\quad\text{and}\quad\hat{\boldsymbol{u}}^T(\hat{r},\tfrac{1}{2}\pi,\phi,\hat{t})=(0,0,0). \tag{11}$$

In the absence of fluid inertia, the purely azimuthal, steady-state viscometric flow between a cone and a disk is given by the velocity field (Bird, Stewart & Lightfoot 1960; Bird *et al.* 1987*a*)

$$\hat{\boldsymbol{u}}_0=[0,0,\Omega\hat{r}g(\theta)]^T, \tag{12}$$

where

$$g(\theta)=\frac{\ln(\tan 1/2\theta)-\cos\theta\operatorname{cosec}^2\theta}{\ln(\tan 1/2\theta_1)-\cos\theta_1\operatorname{cosec}^2\theta_1}\sin\theta, \tag{13}$$

and $\theta_1\equiv\tfrac{1}{2}\pi-\theta_0$. The corresponding components of the polymeric stress field $\hat{\boldsymbol{S}}=\hat{\boldsymbol{S}}_0$ for the Chilcott–Rallison model are

$$\hat{S}_{0rr}=\hat{S}_{0r\theta}=\hat{S}_{0r\phi}=\hat{S}_{0\theta\theta}=0;\quad\hat{S}_{0\theta\phi}=\eta_p\Omega(g'-g\cot\theta), \tag{14}$$

where g' denotes the derivative of the function g with respect to θ. The elastic hoop stress $\hat{S}_{0\phi\phi}$ is determined from the equation

$$\hat{S}_{0\phi\phi}+\frac{2\eta_p\lambda_1\Omega}{f_0}(2\cot\theta\hat{u}_{0\phi}-\hat{u}'_{0\phi})^2=0, \tag{15}$$

where $f_0 \equiv (L^2+\lambda_1 \hat{S}_{0\phi\phi}/\eta_p)/(L^2-3)$ describes the nonlinear force law of the Chilcott–Rallison constitutive model.

Although the velocity and stress fields given by (12)–(15) satisfy the azimuthal component of (10), the $\hat{r}$- and θ-components of the momentum equation cannot be satisfied by this similarity solution. However, for small cone angles, $\theta_0 \ll 1$, an approximate solution can be found (Bird *et al.* 1960; 1987*a*) by expanding $g(\theta)$ in a Taylor series and retaining only the first term in the expansion. The velocity field for torsional flow in the small cone angle limit ($\theta_0 \ll 1$) is then given by

$$\hat{u}_0^T = \left(0, 0, \frac{\frac{1}{2}\pi-\theta}{\theta_0}\Omega\hat{r}\right), \quad 0 \leqslant (\tfrac{1}{2}\pi-\theta) \leqslant \theta_0. \tag{16}$$

In the limit $\theta_0 \ll 1$, the pressure $\hat{p}_0$ and the shear and normal stress components are given by

$$\hat{p}_0 = -\int \frac{\hat{S}_{0\phi\phi}}{\hat{r}}\,\mathrm{d}\hat{r}, \tag{17a}$$

$$\hat{S}_{0\theta\phi} = \eta_p \Omega/\theta_0, \tag{17b}$$

$$\hat{S}_{0\phi\phi} = \frac{\eta_p L^2}{2\lambda_1}\{-1+[1+8(\lambda_1\Omega/\theta_0)^2(L^2-3)/L^4]^{1/2}\}. \tag{17c}$$

The solutions for the velocity and stress components given by (16) and (17) for the limit $\theta_0 \ll 1$ are used as the base state in the disturbance equations for the linear stability analysis of both the Oldroyd-B and Chilcott–Rallison constitutive models. Supplementary calculations for the Oldroyd-B fluid using the full solutions given by (12)–(15) for the azimuthal base state of the velocity field and stress components showed very little ($\leqslant 1\,\%$) difference except at large Deborah numbers and cone angles. Giesekus (1963) and Walters & Waters (1968) have shown that the steady azimuthal viscometric motion described by (16) is accurate for cone angles $\theta_0 \leqslant 10°$ (0.175 rad). For larger cone angles, the steady base motion consists of a primary azimuthal flow and a weak secondary toroidal motion with a magnitude that scales as $\sim Re\, De_0\, \theta_0^2$ which must be incorporated into a self-consistent linear stability analysis.

4.2. *Disturbance equations and solution procedure*

Equations governing the linear stability of the base flow in the transformed coordinates system (ξ, θ, ϕ) are developed using the coordinate transformation defined in §2.3. All variables are made dimensionless by scaling with $(\Omega^{-1}, \hat{r}\Omega, \eta_0\Omega)$ for (time, velocity, stress) respectively. Note that in this formulation there is no characteristic radial lengthscale, and the velocity field at any point is scaled by $\hat{r}\Omega$, where $\hat{r}$ is the local radial coordinate. The disturbances to the velocity, pressure, and stress fields are represented in the form

$$\begin{bmatrix} \tilde{u}_r \\ \tilde{u}_\theta \\ \tilde{u}_\phi \\ \tilde{p} \\ \tilde{S}_{rr} \\ \tilde{S}_{r\theta} \\ \tilde{S}_{r\phi} \\ \tilde{S}_{\theta\theta} \\ \tilde{S}_{\theta\phi} \\ \tilde{S}_{\phi\phi} \end{bmatrix} (\xi, \theta, \phi, t) = \begin{bmatrix} 0 \\ 0 \\ u_{0\phi} \\ p_0 \\ 0 \\ 0 \\ 0 \\ 0 \\ S_{0\theta\phi} \\ S_{0\phi\phi} \end{bmatrix} + \begin{bmatrix} u_r \\ u_\theta \\ u_\phi \\ p \\ S_{rr} \\ S_{r\theta} \\ S_{r\phi} \\ S_{\theta\theta} \\ S_{\theta\phi} \\ S_{\phi\phi} \end{bmatrix} (\xi, \theta, \phi, t), \tag{18}$$

where $(\tilde{u}_r, \tilde{u}_\theta, \tilde{u}_\phi)$ are the dimensionless (radial, meridional, azimuthal) components of the velocity field, $(\tilde{S}_{rr}, \tilde{S}_{r\theta}, \tilde{S}_{r\phi}, \tilde{S}_{\theta\theta}, \tilde{S}_{\theta\phi}, \tilde{S}_{\phi\phi})$ are the components of the polymeric stress, (u_r, u_θ, u_ϕ) are the components of the perturbation to the velocity field, p is the disturbance to the pressure field, and $(S_{rr}, S_{r\theta}, S_{r\phi}, S_{\theta\theta}, S_{\theta\phi}, S_{\phi\phi})$ are the disturbances in the polymer contribution to the extra stress. Here $u_{0\phi}$ is the azimuthal velocity of the base torsional flow, $p_0 \equiv \hat{p}_0/(\eta_0 \Omega)$ is the corresponding pressure, and $S_{0\theta\phi} \equiv \tilde{S}_{0\theta\phi}/(\eta_0 \Omega)$ and $S_{0\phi\phi} \equiv \tilde{S}_{0\phi\phi}/(\eta_0 \Omega)$ are the dimensionless shear and normal stresses, respectively. The dimensionless groups which arise from the scaling of the velocity and stress field in the constitutive equation are the *zero-shear-rate Deborah number*, $De_0 \equiv \lambda_1 \Omega$, and the solvent viscosity ratio $\beta \equiv \eta_s/\eta_0$.

Substituting (18) into (10)–(15) and retaining only terms that are linear in the disturbance amplitude yields the dimensionless disturbance equations and boundary conditions. The continuity and momentum equations for the disturbances are

$$3u_r + \frac{\partial u_r}{\partial \xi} + \frac{\partial u_\theta}{\partial \theta} + \cot\theta\, u_\theta + \operatorname{cosec}\theta \frac{\partial u_\phi}{\partial \phi} = 0, \tag{19a}$$

$$\begin{aligned} &\frac{\partial S_{rr}}{\partial \xi} + 2S_{rr} + \frac{\partial S_{r\theta}}{\partial \theta} + \cot\theta\, S_{r\theta} + \operatorname{cosec}\theta \frac{\partial S_{r\phi}}{\partial \phi} - S_{\theta\theta} - S_{\phi\phi} - \frac{\partial p}{\partial \xi} \\ &\quad + \beta\left(6 + 2\frac{\partial}{\partial \xi} + \frac{\partial^2}{\partial \xi^2} + \cot\theta \frac{\partial}{\partial \theta} + \frac{\partial^2}{\partial \theta^2} + \operatorname{cosec}\theta \frac{\partial^2}{\partial \phi^2}\right) u_r = 0, \end{aligned} \tag{19b}$$

$$\begin{aligned} &3S_{r\theta} + \frac{\partial S_{r\theta}}{\partial \xi} + \cot\theta\, S_{\theta\theta} + \frac{\partial S_{\theta\theta}}{\partial \theta} + \operatorname{cosec}\theta \frac{\partial S_{\theta\phi}}{\partial \phi} - \cot\theta S_{\phi\phi} - \frac{\partial p}{\partial \theta} \\ &\quad + \beta\left(2 + 3\frac{\partial}{\partial \xi} + \frac{\partial^2}{\partial \xi^2} + \cot\theta \frac{\partial}{\partial \theta} - \operatorname{cosec}^2\theta + \frac{\partial^2}{\partial \theta^2} + \operatorname{cosec}^2\theta \frac{\partial^2}{\partial \phi^2}\right) u_\theta \\ &\quad + 2\beta\left(\frac{\partial u_r}{\partial \theta} - \cot\theta \operatorname{cosec}\theta \frac{\partial u_\phi}{\partial \phi}\right) = 0, \end{aligned} \tag{19c}$$

$$\begin{aligned} &3S_{r\phi} + \frac{\partial S_{r\phi}}{\partial \xi} + \cot\theta\, S_{\theta\phi} + \frac{\partial S_{\theta\phi}}{\partial \theta} + \operatorname{cosec}\theta \frac{\partial S_{\phi\phi}}{\partial \phi} - \cot\theta\, S_{\theta\theta} - \operatorname{cosec}\theta \frac{\partial p}{\partial \phi} \\ &\quad + \beta\left(2 + 3\frac{\partial}{\partial \xi} + \frac{\partial^2}{\partial \xi^2} + \cot\theta \frac{\partial}{\partial \theta} - \operatorname{cosec}^2\theta + \frac{\partial^2}{\partial \theta^2} + \operatorname{cosec}^2\theta \frac{\partial^2}{\partial \phi^2}\right) u_\phi \\ &\quad + 2\beta \operatorname{cosec}\theta\left(\frac{\partial u_r}{\partial \phi} + 2\cot\theta \frac{\partial u_\theta}{\partial \phi}\right) = 0. \end{aligned} \tag{19d}$$

The linearized components of the constitutive equations are

$$\mathrm{H}S_{rr} = 2\beta_p(u_r + \partial u_r/\partial \xi), \tag{20a}$$

$$\mathrm{H}S_{r\theta} - De\, S_{0\theta\phi} \operatorname{cosec}\theta \frac{\partial u_r}{\partial \phi} = \beta_p\left(\frac{\partial u_\theta}{\partial \xi} + \frac{\partial u_r}{\partial \theta}\right), \tag{20b}$$

$$\mathrm{H}S_{r\phi} + De\left(u_{0\phi} \cot\theta\, S_{r\theta} - \frac{\partial u_{0\phi}}{\partial \theta} S_{r\theta} - S_{0\theta\phi} \frac{\partial u_r}{\partial \theta} - S_{0\phi\phi} \operatorname{cosec}\theta \frac{\partial u_r}{\partial \phi}\right) = \beta_p\left(\frac{\partial u_\phi}{\partial \xi} + \operatorname{cosec}\theta \frac{\partial u_r}{\partial \phi}\right) \tag{20c}$$

$$\mathrm{H}S_{\theta\theta}-2De\,S_{0\theta\phi}\operatorname{cosec}\theta\frac{\partial u_\theta}{\partial\phi}=2\beta_p\left(\frac{\partial u_\theta}{\partial\theta}+u_r\right), \tag{20d}$$

$$(\mathrm{H}+\tilde{\mathrm{H}})\,S_{\theta\phi}+De\,S_{\theta\theta}\left(\cot\theta u_{0\phi}-\frac{\partial u_{0\phi}}{\partial\theta}\right)-De\,S_{0\theta\phi}\left(\operatorname{cosec}\theta\frac{\partial u_\phi}{\partial\phi}+\cot\theta\,u_\theta+\frac{\partial u_\theta}{\partial\theta}+2u_r\right)$$
$$-De\,S_{0\phi\phi}\operatorname{cosec}\theta\frac{\partial u_\theta}{\partial\phi}=\beta_p\left(\frac{\partial u_\phi}{\partial\theta}+\operatorname{cosec}\theta\frac{\partial u_\theta}{\partial\phi}-\cot\theta\,u_\phi\right), \tag{20e}$$

$$(\mathrm{H}+\tilde{\mathrm{H}})\,S_{\phi\phi}+2De\,S_{\theta\phi}\left(\cot\theta\,u_{0\phi}-\frac{\partial u_{0\phi}}{\partial\theta}\right)-2De\,S_{0\phi\phi}\left(\operatorname{cosec}\theta\frac{\partial u_\phi}{\partial\phi}+\cot\theta\,u_\theta+u_r\right)$$
$$+\tilde{\mathrm{H}}(S_{rr}+S_{\theta\theta}+S_{\phi\phi})+2De\,S_{0\theta\phi}\left(\cot\theta\,u_\phi-\frac{\partial u_\phi}{\partial\theta}\right)=2\beta_p\left(\operatorname{cosec}\theta\frac{\partial u_\phi}{\partial\phi}+u_r+\cot\theta\,u_\theta\right), \tag{20f}$$

where the operators $\mathrm{H}(\cdot)$ and $\tilde{\mathrm{H}}(\cdot)$ are defined by

$$\mathrm{H}(\cdot)\equiv 1+De\left(\frac{\partial}{\partial t}+u_r\frac{\partial}{\partial\xi}+u_\theta\frac{\partial}{\partial\theta}+u_\phi\operatorname{cosec}\theta\frac{\partial}{\partial\phi}\right), \tag{20g}$$

$$\tilde{\mathrm{H}}(\cdot)\equiv-\frac{De^2}{\beta_p(L^2+3)}\left(\frac{\partial}{\partial t}+f_0\operatorname{cosec}\theta\frac{\partial}{\partial\phi}\right). \tag{20h}$$

The dimensionless polymeric contribution to the viscosity is written as $\beta_p\equiv(1-\beta)$ and the modified or 'apparent' Deborah number in the disturbance equations is defined by $De\equiv De_0/f_0$. Since $f_0\geqslant 1$ for all finite extensibilities L, the nonlinearities in the constitutive model serve to reduce the relative importance of the destabilizing viscoelastic terms in the disturbance equations by decreasing the modified Deborah number.

The boundary conditions on the disturbance velocity are

$$\boldsymbol{u}^T(\xi,\theta,\phi,t)=\boldsymbol{0}\quad\text{at}\quad\theta=\tfrac{1}{2}\pi-\theta_0\quad\text{and}\quad\theta=\tfrac{1}{2}\pi. \tag{21}$$

Note that because of the coordinate transformation, (19) and (20) are separable in ξ- and ϕ-coordinates. In contrast to the linear stability analysis for the viscoelastic flow between the parallel rotating disks described previously by Öztekin & Brown (1993) and BÖBM, the restriction of localizing disturbances to a fixed radial location is not required. The spatial dependence of each disturbance equation can be separated, and in fact becomes independent of ξ, if the disturbances in (19) and (20) are decomposed in the normal mode representation $A(\theta)\exp(\mathrm{i}\alpha_\xi\xi+\mathrm{i}m\phi+\sigma t)$, where the constants are defined after (3), and $A(\theta)$ is a complex amplitude function that satisfies the boundary conditions at the upper and lower plates.

For the Oldroyd-B model, we follow the Galerkin/Chebyshev method described by Öztekin & Brown (1993) for the viscoelastic flow between rotating coaxial parallel disks. Substituting this form into (19) and (20) and eliminating the pressure and stress components from 19(b)–19(d) using 19(a) and (20) yields a set of equations which can be represented in the form

$$\sum_{n=0}^{4}P^n\left(\sum_{k=0}^{4}a_{nk}(\alpha_\xi,m,De_0,\theta_0,\beta)\,\mathrm{D}^k\,U_\theta+\sum_{j=0}^{2}b_{nj}(\alpha_\xi,m,De_0,\theta_0,\beta)\,\mathrm{D}^j\omega\right)=0, \tag{22}$$

$$\sum_{n=0}^{4}P^n\left(\sum_{k=0}^{4}c_{nk}(\alpha_\xi,m,De_0,\theta_0,\beta)\,\mathrm{D}^k\,\omega+\sum_{j=0}^{2}d_{nj}(\alpha_\xi,m,De_0,\theta_0,\beta)\,\mathrm{D}^jU_\theta\right)=0, \tag{23}$$

where $\mathrm{D} \equiv \mathrm{d}/\mathrm{d}\theta$, $P \equiv [1 + De\,\sigma + \mathrm{i}m\,De\,g(\theta)/\sin\theta]$, and $U_\theta(\theta)$ is the amplitude of the meridional (θ) component of the velocity. The function $\omega(\theta)$ is defined as $\omega(\theta) \equiv \mathrm{i}\alpha_\xi U_\phi - \mathrm{i}mU_\xi = \varpi(\theta) - U_\phi$, where $\varpi(\theta)$ is the θ-component of the vorticity and $U_\xi(\theta)$ and $U_\phi(\theta)$ are the amplitudes of the ξ- and θ-components of the disturbance velocity, respectively. For small values of the cone angle, a scaling analysis shows that $\omega(\theta)$ approximates the amplitude of the θ-component of the disturbance vorticity. Equations (22) and (23) are similar to those for the viscoelastic flow of an Oldroyd-B fluid between parallel rotating disks (Öztekin & Brown 1993). Details of the coefficients $a_{nj}(\alpha_\xi, m, De_0, \theta_0, \beta)$, $b_{nj}(\alpha_\xi, m, De_0, \theta_0, \beta)$, $c_{nj}(\alpha_\xi, m, De_0, \theta_0, \beta)$ and $d_{nj}(\alpha_\xi, m, De_0, \theta_0, \beta)$ are available from the authors. The boundary conditions on the linear stability problem are

$$U_\theta(\tfrac{1}{2}\pi) = \mathrm{D}U_\theta(\tfrac{1}{2}\pi) = \omega(\tfrac{1}{2}\pi) = 0, \qquad (24\,a\text{–}c)$$

and

$$U_\theta(\tfrac{1}{2}\pi - \theta_0) = \mathrm{D}U_\theta(\tfrac{1}{2}\pi - \theta_0) = \omega(\tfrac{1}{2}\pi - \theta_0) = 0. \qquad (25\,a\text{–}c)$$

Equations (22)–(25) describe an eigenvalue problem for the growth rate σ and the eigenfunction, composed of $U_\theta(\theta)$ and $\omega(\theta)$, as a function of the spatial wavenumbers (α_ξ, m), and the dimensionless parameters (θ_0, β, De_0). This eigenvalue problem is solved by using a Galerkin/Chebyshev approximation. The details of the numerical technique are described by Öztekin & Brown (1993).

For the nonlinear Chilcott–Rallison constitutive model, the mixed Tau–Galerkin/Chebyshev method is used to solve the eigenvalue problem. Rather than eliminating the stress components from the momentum and constitutive equations as for the Galerkin/Chebyshev method discussed above, the polymeric stress components are discretized using Chebyshev polynomial expansions. The details of this more general method are given in BÖBM.

The Galerkin/Chebyshev and mixed Tau–Galerkin/Chebyshev procedures reduce the system of equations and boundary conditions to generalized matrix eigenvalue problems of the form

$$(\boldsymbol{A} + \sigma\boldsymbol{B})\boldsymbol{x} = 0, \qquad (26)$$

where $\boldsymbol{x} \in \Re^{8(N+1)}$ are the components of the discretized eigenvectors and the elements of the square matrices $\boldsymbol{A}$ and $\boldsymbol{B}$ each in $\Re^{8(N+1)\times 8(N+1)}$ depend on the set of disturbance parameters $(\alpha_\xi, m, L, De_0, \beta)$. The solutions of the eigenvalue and eigenvectors of the algebraic problem (26) are computed using the algorithm DGVCCG available in the IMSL library.

The stability of the viscometric flow is characterized for given De_0 and m by neutral stability curves of $\theta_0 = \theta_0(\alpha_\xi)$ for which $\mathrm{Re}(\sigma) = 0$. These curves are determined by computing the growth rate σ for fixed values of (α_ξ, m, L, De_0) at several values of the cone angle θ_0 and subsequently using bisection to determine the critical value $\theta_{0crit}(\alpha_\xi)$. These searches are carried out to one part in 10^6 for axisymmetric disturbances $(m = 0)$ and to one part in 10^4 for non-axisymmetric disturbances $(m \neq 0)$. The eigenvalues computed for the Oldroyd-B model by either the Galerkin or mixed Tau–Galerkin/Chebyshev methods are identical to at least one part in 10^5.

5. Linear stability results

Stability calculations using the Oldroyd-B and Chilcott–Rallison constitutive models are reported for torsional flow between a rotating infinite cone and stationary plate. Axisymmetric $(m = 0)$ and non-axisymmetric $(m \neq 0)$ disturbances are considered primarily for the specific solvent viscosity ratio of $\beta = 0.59$ corresponding to the value determined for the 0.31 wt% PIB/PB/C14 Boger fluid used in the experiments described in §3. Representative calculations for additional values of the viscosity ratio in the range of $0 \leqslant \beta < 1$ are also discussed briefly. Stability calculations with the Oldroyd-B constitutive model are continued up to $De_0 = 3$, in order to fully explore the variation of the temporal and spatial characteristics of the instabilities with Deborah number. However, computations for the Oldroyd-B model beyond $De_0 \sim 2$ may not be reliable because the critical cone angle for onset of the instabilities becomes greater than 10° and the assumption of a purely azimuthal base flow becomes invalid. Similarly, stability calculations for the Chilcott–Rallison model are limited to critical cone angles less than 15°. For this model, this limit corresponds to Deborah numbers and dumbbell extensibilities in the range $0 \leqslant De_0 \leqslant 7$ and $10 \leqslant L \leqslant \infty$ respectively.

5.1. *Elastic instability in the Oldroyd-B fluid*

Since the linearized stability problem ((22)–(25)) is very similar to the one discussed in BÖBM we do not present our studies of the spectral convergence of the most unstable eigenmode in detail here. As was found in our previous calculations (Öztekin & Brown 1993) for the viscoelastic flow between rotating parallel disks, non-axisymmetric disturbances with larger values of m require higher spectral resolution. The spectrum of the discrete eigenvalue problem for the non-axisymmetric disturbance flow consists of eight continuous branches and a discrete branch. The eigenvalues of the continuous spectrum converge slower than the eigenvalues of the discrete spectrum. The calculations reported in the remainder of this work are based on the values of the discretization, N, for which the most unstable mode in the discrete spectrum is convergent to one part in 10^4 and all of the eigenvalues belonging to the continuous part of the spectrum are stable.

The neutral stability curves computed for axisymmetric ($m = 0$) disturbances with $\beta = 0.59$ are shown in figure 9 for Deborah numbers in the range $0.5 \leqslant De_0 \leqslant 3$. The critical parameter $R^*(\alpha_\xi) \equiv 1/\theta_0(\alpha_\xi)$ plotted on the ordinate is analogous to the dimensionless critical radial position $R^* \equiv \hat{r}_{crit}/H$ defined in BÖBM for the parallel-disk geometry, where $\hat{r}_{crit}$ denotes the dimensional onset radius of the instability and H is the gap between the plates. The neutral stability curves in this paper are presented in terms of the geometric parameter $R^* \equiv 1/\theta_0$ to facilitate the comparison between the parallel-plate and cone-and-plate calculations. For any value of De_0, there is a minimum critical value of the parameter R^* which we denote by $R^*_{crit}(\alpha_{\xi crit})$, or equivalently a maximum critical cone angle $\theta_{0crit}(\alpha_{\xi crit})$ that corresponds to the onset of the elastic instability. For $R^* < R^*_{crit}(\alpha_{\xi crit})$, or equivalently $\theta_0 > \theta_{0crit}(\alpha_{\xi crit})$, the viscometric flow is stable for all values of the wavenumber α_ξ, whereas for $R^* > R^*_{crit}(\alpha_{\xi crit})$, or $\theta_0 < \theta_{0crit}(\alpha_{\xi crit})$, the flow is unstable to disturbances in some range of α_ξ. Decreasing the Deborah number De_0 raises the stability locus $R^*_{crit}(\alpha_\xi, De_0)$, making the flow *more stable* in the sense that instability starts at a smaller cone angle, or a higher value of the shear rate $\dot{\gamma} = \Omega/\theta_0$.

From figure 9 it is also seen that the most dangerous wavenumber α_ξ in the transformed domain (ξ, θ, ϕ) increases with decreasing De_0, and is always much larger than the values $3 \leqslant \alpha \leqslant 4$ determined in BÖBM for the parallel-plate instability. The 'wiggles' observed on the high-α_ξ side of each neutral curve arise from a switching in the value of the most unstable discrete eigenmode. A very similar behaviour is observed in the stability curves for viscoelastic flow between parallel plates (cf. Öztekin & Brown 1993, figure 3).

Non-axisymmetric disturbances correspond to Archimedean spirals in the transformed domain (ξ, θ, ϕ) and thus have a representation similar to the non-axisymmetric disturbances between parallel rotating disks analysed in BÖBM. The neutral stability curves $R^* = R^*(\alpha_\xi, m) \equiv 1/\theta_0$ for $\beta = 0.59$ and two representative

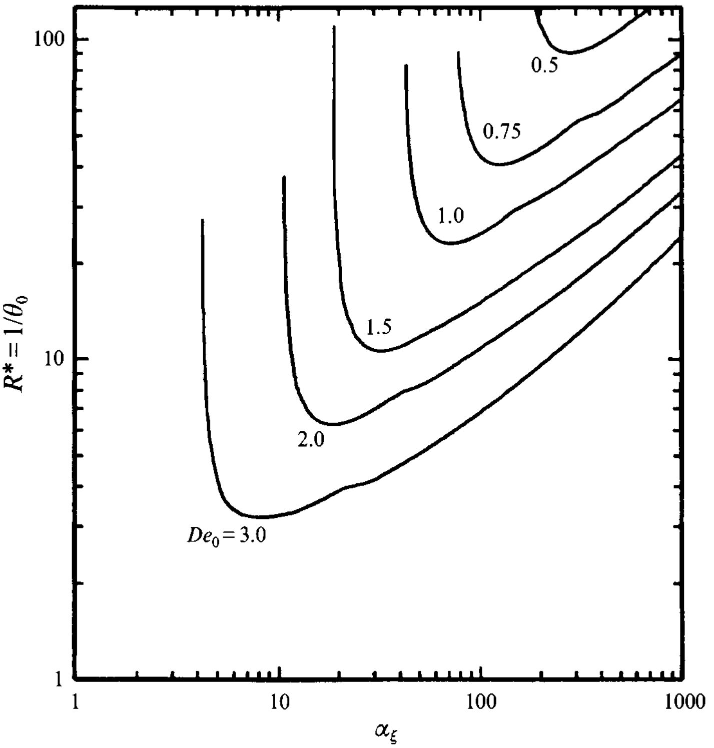

FIGURE 9. The neutral stability curves $R^* \equiv 1/\theta_0(\alpha_\xi)$ computed for axisymmetric disturbances ($m = 0$) to the Oldroyd-B model with $\beta = 0.59$, for Deborah numbers in the range $0.5 \leqslant De_0 \leqslant 3.0$.

Deborah numbers, $De_0 = 1$ and 2, are shown in figure 10 for $-5 \leqslant m \leqslant 5$. The neutral curves and critical cone angle for the outward-winding (positive angle) and inward-winding (negative angle) spirals are almost the same for each value of De_0, as found previously by BÖBM. At $De_0 = 2$, the lowest value of $R^* = R^*_{crit}(\alpha_{\xi crit}, m)$ occurs for the non-axisymmetric modes ($m = \pm 2$), corresponding to a spiral winding number of $n_{crit} = \pm 0.02$. The differences between the critical values of the parameter $R^*_{crit}(\alpha_{\xi crit}, m)$ are very small for the $m = 0$ and $m = \pm 2$ modes, but slightly larger between the $m = -1$ and $m = 0$ or $m = -2$ modes. The most dangerous wavenumbers $\alpha_{\xi crit}$ for the $m = 0$ and $m = -2$ modes are approximately the same, while the critical wavenumber for the $m = -1$ mode shifts to a larger value. Decreasing the Deborah number to $De_0 = 1$ shifts the relative ordering of the different modes and the critical disturbances are non-axisymmetric spirals with $m = \pm 4$ as shown in figures 10(*c*) and 10(*d*).

Again it can be noted that lowering the Deborah number increases the critical wavenumber $\alpha_{\xi crit}$ and decreases the critical cone angle θ_{0crit} for onset of instability. To see that this change corresponds to an *increase* in the stability of the base torsional shear flow it is beneficial to introduce another dimensionless group, the *Weissenberg number*. This parameter represents the dimensionless ratio of the elastic normal stresses ($\hat{S}_{0\phi\phi}$) to twice the polymeric shear stress ($\hat{S}_{0\theta\phi}$) in the base shearing flow (Bird *et al.* 1987*a*; Larson 1992); for the Oldroyd-B model, the Weissenberg number We is thus

$$We \equiv \lambda_1 \dot{\gamma} = (De_0/\theta_0) = De_0 R^*, \qquad (27)$$

and increases linearly with increasing shear rate. Using this definition, it is easily seen that even though the Deborah number decreases by a factor of two from figure 10(*a*)

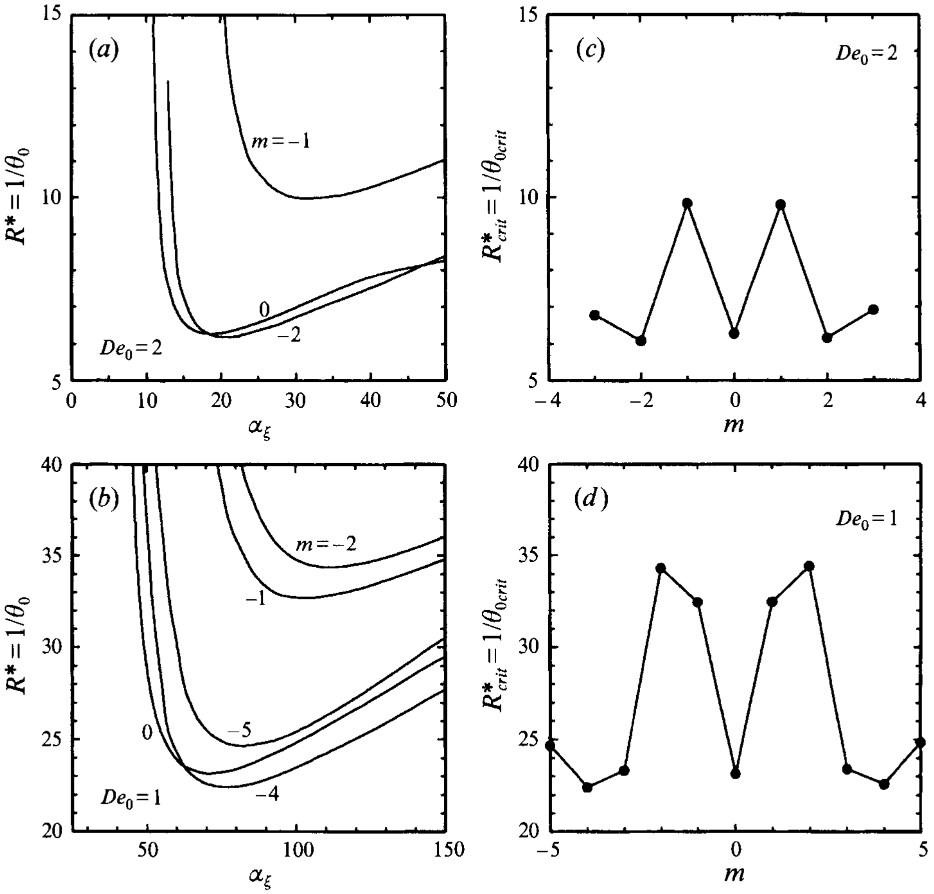

FIGURE 10. The neutral stability curves for non-axisymmetric disturbances of spiral form to the homogeneous base torsional flow of the Oldroyd-B model: (*a*, *b*) Ordering of the neutral stability envelopes $R^*(\alpha_\xi, m) = 1/\theta_0(\alpha_\xi, m)$ for azimuthal modes with $m = 0, -1, \ldots, 5$ at Deborah numbers of $De_0 = 2$ and 1 respectively. (*c*, *d*). The critical cone angle (θ_{0crit}), represented in terms of the parameter $R^*_{crit} \equiv 1/\theta_{0crit}(\alpha_{\xi crit})$, for onset of instability for azimuthal modes with $-5 \leqslant m \leqslant 5$ at the same Deborah numbers.

to 10(*b*), the critical Weissenberg number for onset of instability, $We_{crit} = De_0 R^*_{crit}$, *increases* – indicating a higher critical shear rate for onset of the elastic instability.

Contours of the eigenfunction corresponding to the magnitude of the meridional disturbance velocity U_θ in the (ξ, θ)-plane are shown in figure 11 over the period of one wavelength for both the axisymmetric $(m = 0)$ and the $m = \pm 4$ non-axisymmetric disturbances. These eigenfunctions are computed for the critical values of the cone angle $\theta_{0crit}(\alpha_{\xi crit})$ calculated at $De_0 = 1$ for each mode with $\beta = 0.59$. The eigenfunction structures are again very similar to those computed in our earlier work for torsional flows between rotating parallel disks. The velocity eigenfunction for the axisymmetric disturbance is symmetric about the midplane, $\theta_{mid} = \frac{1}{2}(\pi - \theta_0)$, between the cone and plate, whereas the non-axisymmetric velocity eigenfunction is skewed in the ξ-direction. The maximum amplitude of the axisymmetric disturbance velocity is obtained at the midplane while the non-axisymmetric velocity disturbances have maxima closer to the stationary plate for the $m = 4$ mode and to the rotating cone for the complementary $m = -4$ mode.

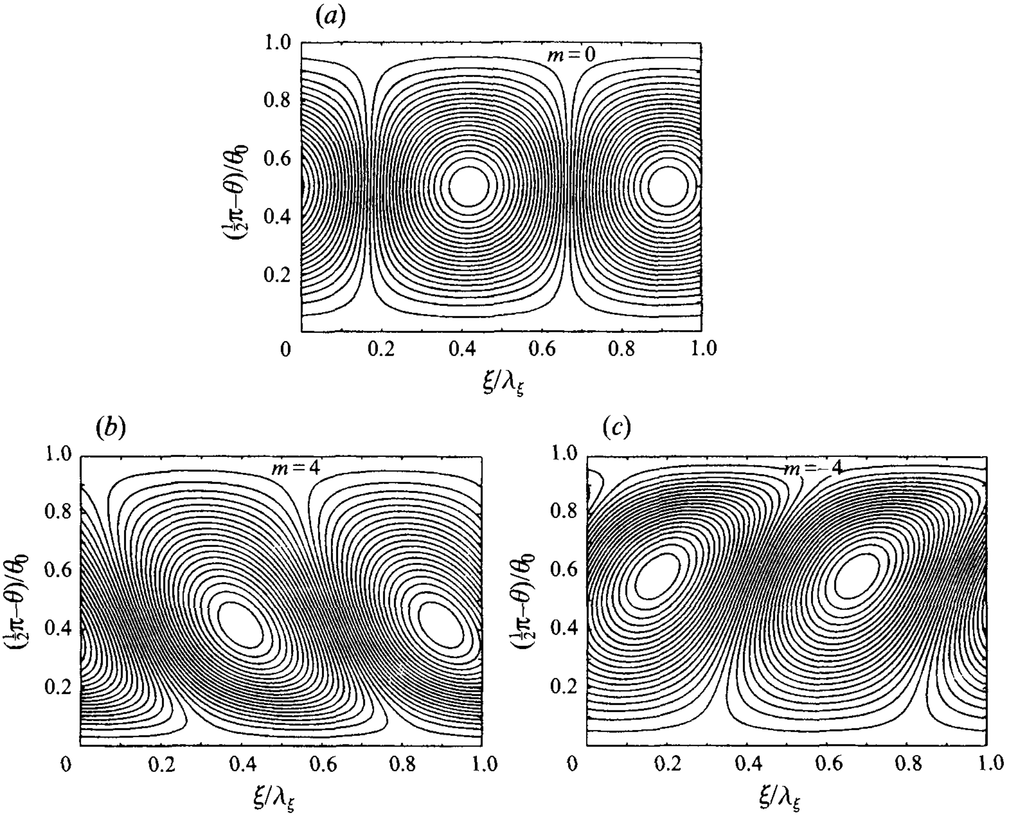

FIGURE 11. Contours of the eigenfunctions describing the disturbance to the meridional velocity U_θ with $\beta = 0.59$ and $De_0 = 1$ for (*a*) the axisymmetric mode ($m = 0$), (*b*) the positive-angle $m = 4$ mode and (*c*) the negative-angle $m = -4$ non-axisymmetric disturbance mode.

Extensive calculations for different values of the solvent viscosity ratio, β, have been performed in order to systematically explore the effects of rheological variations on this elastic cone-and-plate instability. These calculations show that the precise ordering of the azimuthal mode structure and the critical rotation rate for onset of instability are very sensitive functions of the magnitude of the solvent viscosity. These results are concisely summarized in figure 12, where the variation in the critical value of the cone angle for the onset of the axisymmetric and the most dangerous non-axisymmetric disturbances is plotted in terms of the critical Weissenberg number $We_{crit} \equiv De_0/\theta_{0crit}(\alpha_{\xi crit})$ for Deborah numbers in the range $0.5 \leqslant De_0 \leqslant 2$. The mode number of the most dangerous non-axisymmetric disturbance varies with the critical cone angle, and the value of m corresponding to the most unstable mode at each set of conditions is shown in figure 12(*b*). In the linear analysis, the critical conditions for positive- and negative-angle spirals are approximately the same at each point and are represented in terms of the magnitude $M_{crit} = |m_{crit}|$. For each value of De_0, the axisymmetric disturbances are the most dangerous for solvent viscosity ratios above 0.6; below this value, non-axisymmetric disturbances are most unstable and the azimuthal wavenumber increases as the Deborah number decreases. For the value $\beta = 0.59$, the non-axisymmetric disturbances are the most dangerous but the spacing between different modes is very small. As the solvent contribution is reduced towards the limit of an Upper-Convected Maxwell model ($\beta = 0$), the differences in the values

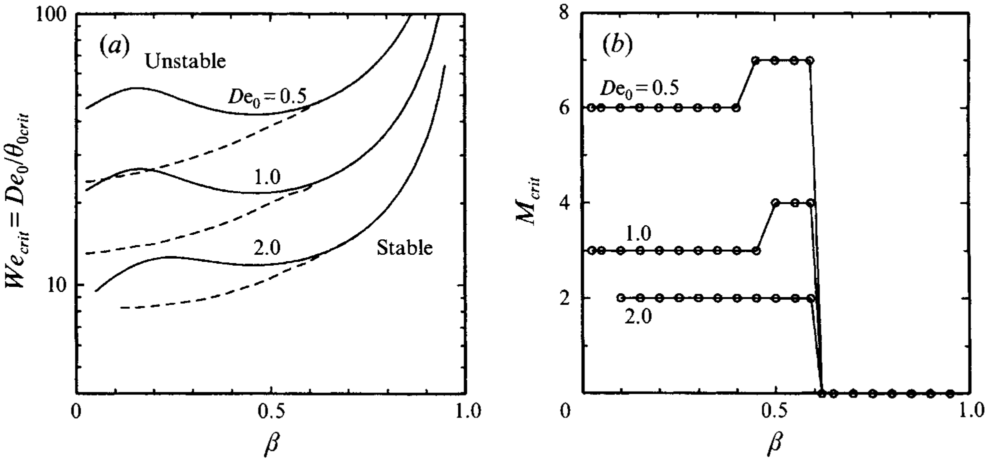

FIGURE 12. Variation with solvent viscosity ratio of (*a*) the critical Weissenberg number $We_{crit}(\beta)$ for the onset of the axisymmetric (——) and the most dangerous disturbance (– – – –) modes, and of (*b*) the magnitude of the azimuthal mode number corresponding to the most dangerous disturbance $M_{crit}(\beta)$ for $De_0 = 0.5$, 1 and 2.

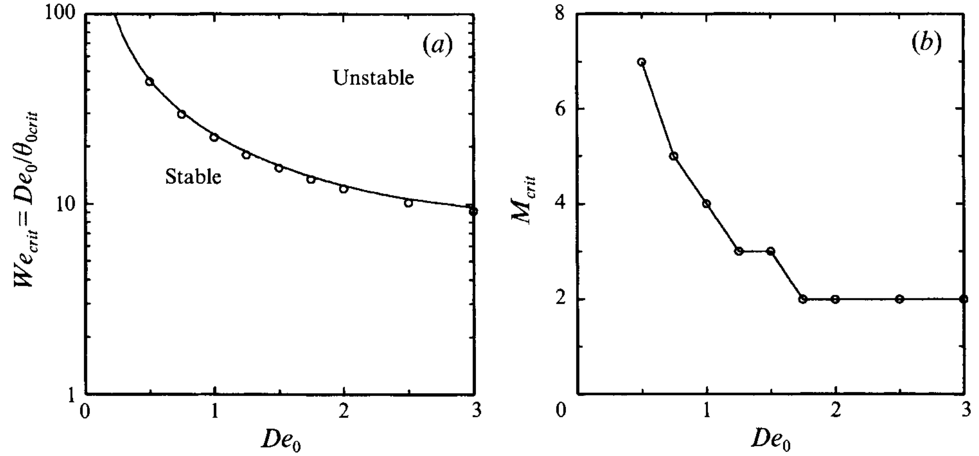

FIGURE 13. Stability diagram for spiral instabilities in torsional flow of the Oldroyd-B model between a cone and a plate, $\beta = 0.59$; (*a*) the critical Weissenberg number We_{crit} for the onset of both axisymmetric (——) and the most dangerous (○) disturbance modes, and (*b*) the azimuthal mode number, $M_{crit}(De_0)$, corresponding to the most unstable disturbance.

of the critical Weissenberg number for the axisymmetric and the most dangerous non-axisymmetric modes becomes more appreciable. In the Newtonian limit, $\beta \to 1$, the critical Weissenberg number for onset of instability approaches infinity, i.e. the base flow becomes stable for all disturbances, as expected for creeping torsional motion of a Newtonian fluid.

A stability diagram for the torsional flow of an Oldroyd-B fluid in cone-and-plate geometries with different cone angles can be constructed from a series of calculations for each value of the solvent viscosity ratio β. The variation of $We_{crit} \equiv De_0/\theta_{0crit}$ with Deborah number is shown in figure 13 for both axisymmetric and the most dangerous non-axisymmetric disturbances. The axisymmetric disturbance is never the most unstable; however, the difference in the critical cone angle (or critical Weissenberg number) for axisymmetric and most dangerous non-axisymmetric modes is very small for all De_0. The integer value of $M_{crit} = |m_{crit}|$ that corresponds to the most dangerous disturbance is plotted in figure 13(*b*) as a function of De_0. As the Deborah number is decreased, the critical Weissenberg number increases and non-axisymmetric disturbances with higher values of m become progressively more unstable.

For the purpose of completeness, it is also worth considering the location on such a diagram of the Phan-Thien stability boundary for axisymmetric disturbances of von Kármán similarity form, calculated using the corrected expression given by Olagunju & Cook (1993). This analytic stability criterion depends on the solvent viscosity ratio β in the Oldroyd-B model but unlike the analysis presented here is *independent* of the cone angle θ_0. The neutral stability curve will thus be a vertical line, and for a fluid with $\beta = 0.59$ and $Re \ll 1$ the critical Deborah number is calculated to be $De_{crit}^{(PT)} = 3.55$. In experiments with a viscoelastic fluid that is accurately modelled by the Oldroyd-B constitute equation, instabilities of spiral form will therefore be the more unstable modes of disturbance unless the Weissenberg number is kept rather small. This corresponds to large values of the cone angle ($\theta_0 \approx 25°$), and it is not clear whether the purely azimuthal base flow considered by either analysis is valid at such conditions.

5.2. *Comparison of Oldroyd-B calculations with experiments*

In this section we present a quantitative comparison of the predictions of the linear stability calculations using the Oldroyd-B model with our experimental observations in the 0.31 wt% PIB/PB/C14 Boger fluid. The critical value of the wavenumbers $\alpha_\xi = \alpha_{\xi crit}(\theta_0)$ and $c_\xi = c_{\xi crit}(\theta_0)$ determined from experiments and predicted by linear stability analysis for the axisymmetric ($m = 0$) and non-axisymmetric disturbances with $m = -1$, -2 and -3 are shown in figure 14. As the cone angle decreases, the wavenumber steadily increases, and the experimental observations and numerical calculations for the critical wavenumber are in excellent quantitative agreement. Additionally, the calculations show that the values of the critical wavenumber of each mode are similar for all cone angles and also that these values become very large as the cone angle approaches zero. The measured and calculated values of the radial wave speed of the disturbance also agree well for the smallest cone angle of $\theta_0 = 6°$; however, for larger cone angles the wave speed of the logarithmic spirals observed in experiments is smaller than the predicted value for any mode. This discrepancy at larger cone angles might be expected since both our experimental and numerical assumptions of a purely azimuthal base flow become inaccurate for cone angles beyond $\theta_0 > 10°$. The linear stability analysis also predicts that the concentric waves ($m = 0$) travel faster than the non-axisymmetric $m = -1$, -2 and -3 logarithmic spirals and that the wave speed of the recirculating vortices decreases as the cone angle is progressively reduced.

The Oldroyd-B model thus appears to provide an accurate description of the spatial form of the elastic instability in cone-and-plate flows. However, in the previous work of BÖBM and Öztekin & Brown (1993) it was noted that under the typical flow conditions attained at onset of these elastic instabilities, Boger fluids actually exhibit shear-rate-dependent material properties; most notably, the first normal stress coefficient $\Psi_1(\dot{\gamma})$ decreases monotonically as a function of increasing shear rate. Construction of an experimental stability diagram and quantitative comparison of critical flow conditions at the onset of the elastic instability therefore requires the definition of an appropriate relaxation time for the test fluid. The Oldroyd-B fluid model of course does not predict any shear-rate dependence in the viscometric properties; however, an *ad hoc* comparison between experiments and linear stability calculations can be effected by defining an 'apparent relaxation time' (McKinley *et al.*

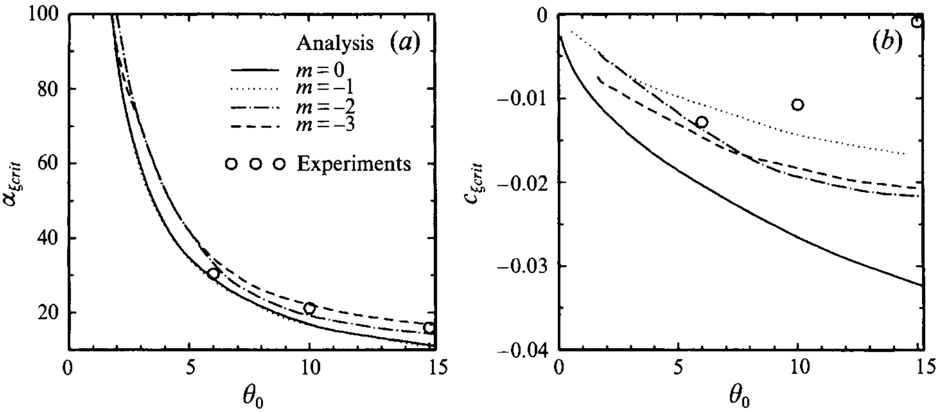

FIGURE 14. Comparison of experimental measurements and predictions from linear stability calculations with the Oldroyd-B model ($\beta = 0.59$) for (a) the dimensionless wavenumber α_ξ, and (b) the dimensionless wave speed c_ξ.

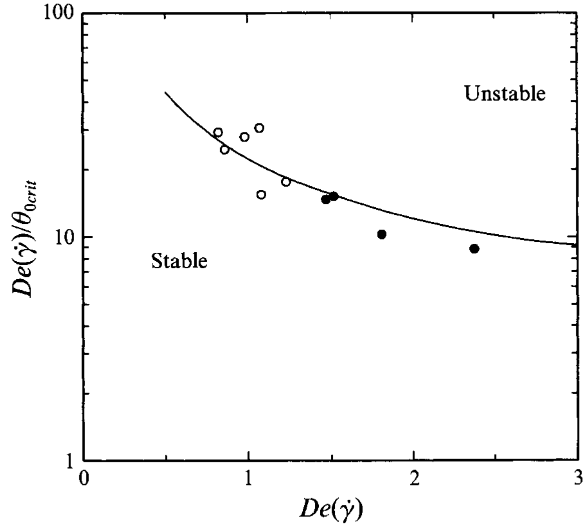

FIGURE 15. Stability diagram for the onset of the elastic instabilities in a cone-and-plate rheometer in terms of the shear-rate-dependent critical Weissenberg number: ●, present experiments with 0.31 wt% PIB/PB/C14 Boger fluid; ○, earlier experiments for M1 Boger fluid; ——, most unstable mode predicted by linear stability analysis with Oldroyd-B model ($\beta = 0.59$).

1991; Larson, Muller & Shaqfeh 1993) as $\lambda_1(\dot{\gamma}) \equiv \Psi_1(\dot{\gamma})/2[\eta(\dot{\gamma}) - \eta_s]$. In this fashion, the actual values of the viscosity and first normal stress coefficient for the fluid are used to construct a new, Oldroyd-like time constant locally at each value of the shear rate in the steady base state. This definition has the correct zero-shear-rate asymptote given in table 1 and, because we are only concerned with linear stability calculations involving infinitesimal perturbations about the base state, we may expect spatial variations in the apparent relaxation time of the fluid sample to be very small at onset of instability.

A direct comparison of the experimentally determined and numerically predicted stability diagram for onset of the elastic spiral instability in cone-and-plate rheometers is presented in figure 15. The shear-rate-dependent relaxation time $\lambda_1(\dot{\gamma})$ is used to calculate an 'apparent critical Deborah number' $De_{crit}(\dot{\gamma}) \equiv \lambda_1(\dot{\gamma})\,\Omega_{crit}$ and an 'apparent critical Weissenberg number' $We_{crit}(\dot{\gamma}) \equiv [De(\dot{\gamma})/\theta_0]_{crit}$ for onset of instability in the Boger fluid, and these values are compared with linear stability calculations for the most unstable disturbance mode predicted using the Oldroyd-B model with $\beta = 0.59$. This critical Weissenberg number corresponds to either the critical dimensionless shear rate that must be achieved for onset of instability in a series of experiments with a fixed conical fixture, or alternatively to the critical cone angle that must be used in linear stability calculations at a fixed Deborah number.

In addition to our own observations with the 0.31 wt% PIB Boger fluid, we also indicate by hollow circles in figure 15 similar data extracted from the recent rheological studies of the 'M1' international test fluid (Hudson & Ferguson 1990; Laun & Hingmann 1990; Steiert & Wolff 1990). This is another polyisobutylene-based Boger fluid containing 0.244 wt% PIB in polybutene and kerosene, with a similar value of the solvent viscosity ratio $\beta_{M1} = 0.52$ (Laun & Hingmann 1990). In these earlier studies using cone-and-plate rheometers with cone angles in the range $1° \leqslant \theta_0 \leqslant 4°$ the flow instability was interpreted in terms of a 'critical shear stress' for structure formation. No information was given about the spatial and temporal characteristics of the instabilities observed in the 'M1' fluid; however, it appears likely that the instability is identical to the travelling logarithmic spiral vortices observed in the current investigation and is better interpreted in terms of a critical Deborah number. It is clear from figure 15 that the agreement between the experiments and theory for the prediction of onset of the elastic cone-and-plate instability is good for both our PIB/PB/C14 fluid and the 'M1' Boger fluid.

5.3. *Linear stability of the Chilcott–Rallison constitutive model*

Although the above discussions have shown that linear stability calculations with the Oldroyd-B constitutive equation capture the correct spatial form of the disturbance kinematics observed in our Boger fluid experiments, a number of experimental observations indicate that the physics contained in this model are insufficient to fully describe the elastic instability. Most notable of these include the absence of instability observed in experiments with a 4° cone up to $De_0 = 8.31$ (cf. table 1), and the necessity of adjusting the experimental measurements using the concept of an 'apparent relaxation time' (§5.2). In BÖBM we showed that similar effects in the parallel-plate geometry can arise from shear thinning of the elastic normal stresses in the experimental test fluids. We therefore proceed in the same manner and consider the stability of the Chilcott–Rallison model (equation (1)) to linearized disturbances of logarithmic spiral form.

Although the base state shear rate, $\dot{\gamma} = \Omega/\theta_0$, in the cone-and-plate geometry is uniform throughout the device, the destabilizing elastic hoop stress in the Chilcott–Rallison model is a nonlinear function of the shear rate (cf. 17(*c*)) and increases at a slower rate than the quadratic variation predicted by the Oldroyd-B constitutive equation. At a fixed value of the zero-shear-rate Deborah number De_0 and large shear rates (i.e. for *very small* cone angles), the elastic hoop stress $\hat{S}_{0\phi\phi}$, and therefore the dimensionless Weissenberg number, predicted by the nonlinear model is smaller than that given by the Oldroyd-B model. The extent of the shear thinning in the elastic stresses increases as the dumbbell extensibility L is decreased, and the 'apparent Deborah number' $De \equiv De_0/f_0$ in the disturbance equations (2) is progressively decreased. This variation has a pronounced influence on the neutral stability curves and stability diagrams presented below.

The neutral stability curves $R^*(\alpha_\xi) \equiv 1/\theta_0(\alpha_\xi)$ for axisymmetric disturbances ($m = 0$) of the Chilcott–Rallison model with a solvent viscosity ratio of $\beta = 0.59$ are shown in

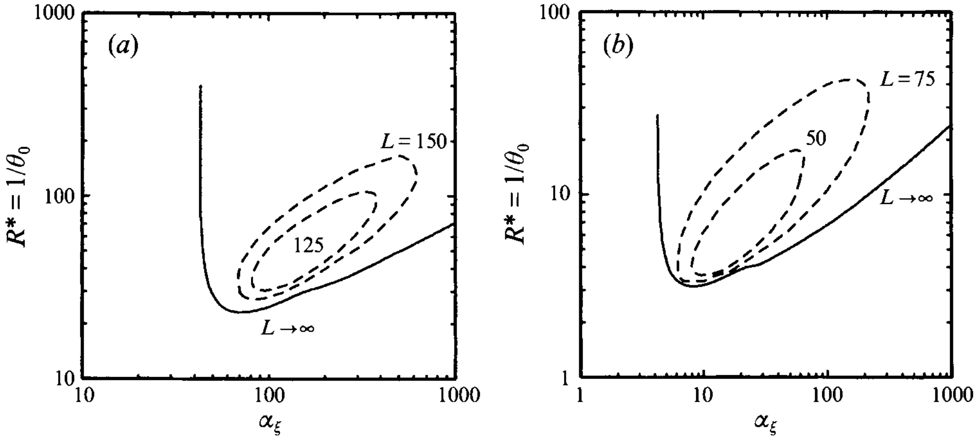

FIGURE 16. Neutral stability curves for axisymmetric disturbances to the Chilcott–Rallison model with $\beta = 0.59$ and for various values of the dumbbell extensibility parameter L at (*a*) $De_0 = 1$, (*b*) $De_0 = 3$.

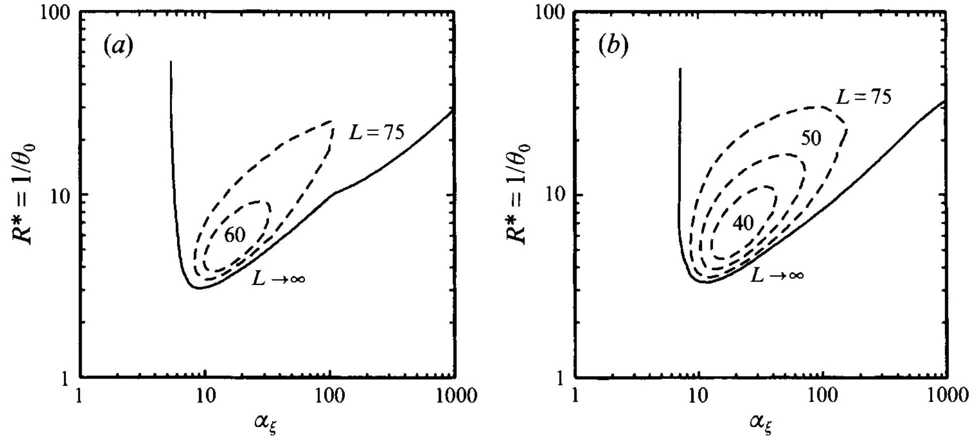

FIGURE 17. Neutral stability curves for non-axisymmetric disturbances to the Chilcott–Rallison model at $De_0 = 3$ for $\beta = 0.59$ and (*a*) $m = -1$, (*b*) $m = -2$.

figure 16 for a range of representative values of the extensibility parameter L. The solid curve in each plot represents the neutral stability curves in the Oldroyd-B fluid limit ($L \to \infty$) that have been discussed above in §5.1. The characteristics of the neutral stability curves for the Chilcott–Rallison model are very different; the locus of neutrally stable points (i.e. where $\mathrm{Re}(\sigma) = 0$) forms a closed loop, and hence the viscometric base motion is only unstable for a finite range of cone angles $\theta_{0crit_1}(\alpha_{\xi crit_1}) > \theta_0 > \theta_{0crit_2}(\alpha_{\xi crit_2})$ at each value of the extensibility parameter L. The values of $R^*_{crit_1} \equiv 1/\theta_{0crit_1}$ and $R^*_{crit_2} \equiv 1/\theta_{0crit_2}$ are, respectively, the minimum and maximum of each neutral stability curve. As L decreases and the nonlinearity in the FENE spring increases, shear thinning in the elastic hoop stresses becomes increasingly important and the unstable region becomes progressively smaller until it eventually disappears completely below a critical value of the extensibility L. It can be seen from comparisons of figures 16(*a*) and 16(*b*) that increasing the Deborah number increases the destabilizing elastic stresses and a smaller critical value of L is required to restabilize the base flow over all values of cone angle.

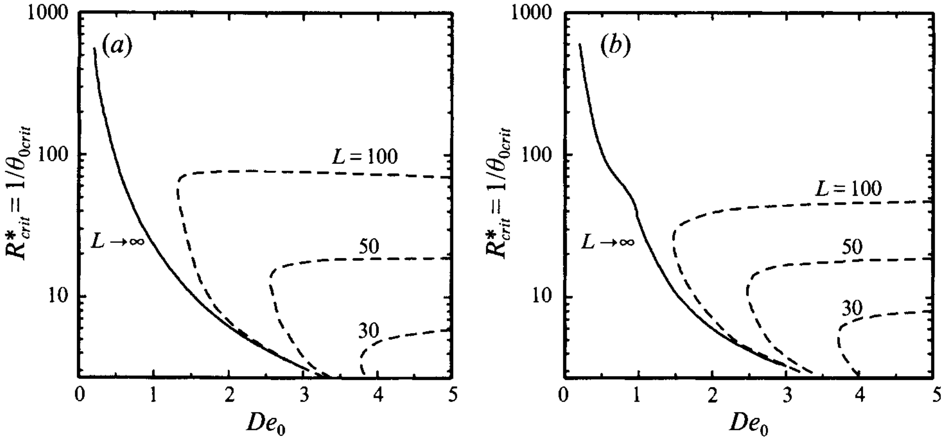

FIGURE 18. Stability diagrams for onset of logarithmic spiral disturbances in the Chilcott–Rallison model ($\beta = 0.59$) with spiral mode (*a*) $m = 0$, (*b*) $m = -2$.

Similar results are obtained by considering non-axisymmetric disturbances. The neutral stability curves $R^*(\alpha_\xi; m) \equiv 1/\theta_0(\alpha_\xi; m)$ for the azimuthal $m = -1$ and $m = -2$ disturbances are shown in figure 17 at a fixed Deborah number of $De_0 = 3$. There is again a finite range of cone angles for which the viscometric flow is unstable, and as L decreases this unstable range becomes smaller and disappears completely beyond a critical value of L. The stabilization due to the shear thinning of the elastic stresses is stronger for the $m = -1$ non-axisymmetric disturbances than for either the $m = -2$ or the $m = 0$ modes.

Stability diagrams for axisymmetric and non-axisymmetric disturbances to the Chilcott–Rallison model are determined by calculating the critical cone angles at which the base flow is destabilized for each value of De_0 and L. The results of such calculations are shown in figure 18. In the Oldroyd-B limit ($L \to \infty$), a finite value of the critical cone angle is predicted for any non-zero value of the Deborah number. For large cone angles (and therefore small shear rates) the stability curves of the Chilcott–Rallison model closely follow the Oldroyd-B stability loci. However, the curves diverge as the critical cone angle decreases and shear-thinning effects in the fluid become increasingly important. For finite values of the extensibility L there exists a critical value of the Deborah number (corresponding to the turning point in each of the curves plotted in figure 18) below which the base flow is stable *for all cone angles*. For $De_0 > De_{0crit}$, the base flow is unstable over the finite range of cone angles $\theta_{0crit_1} > \theta_0 > \theta_{0crit_2}$, but at lower values of the Deborah number, the base torsional motion between a plate and a cone of any angle is stable to all axisymmetric and non-axisymmetric disturbances of spiral form. Of course, this is subject to the important caveat that the purely azimuthal base flow is a valid approximate solution to the inertialess equations of motion. This requires that $\theta_0 < 10°$ (0.173 rad), or equivalently $R^* > 5.7$.

The value of De_{0crit} increases and the range of unstable cone angles shrinks for both the axisymmetric and non-axisymmetric disturbances as the extensibility L is decreased. At large Deborah numbers the variation in the upper stability boundary $R^*_{crit_2} \equiv 1/\theta_{0crit_2}$ with De_0 is weak for all values of L and m, since the rate of shear thinning in the normal stresses asymptotically approaches $\dot{\gamma}^{-1}$. Increasing the Deborah number thus results in almost no change in the destabilizing elastic stresses predicted by the

Chilcott–Rallison model. A similar result was obtained in BÖBM for the elastic parallel-plate instability.

Although it is difficult to discern from figure 18, a detailed comparison of the stability boundaries for different values of L and m shows that for $\beta = 0.59$ the axisymmetric mode is never the most unstable for any dumbbell extensibility $L \leqslant 50$; however, the difference in the critical cone angle for the axisymmetric and non-axisymmetric disturbances is very small. Changing the solvent viscosity ratio results in a reordering of the disturbance modes, as we found previously for the Oldroyd-B model (cf. figure 11). For $\beta = 0.84$ we find that the axisymmetric mode is the most unstable for all values of the Deborah number and the dumbbell extensibility. The stability boundaries exhibit the same general shape as those shown in figure 18 with a turning point corresponding to a minimum critical Deborah number for onset of the elastic instability. However, as the contribution of the stabilizing Newtonian solvent viscosity increases, the overall stability of the purely azimuthal flow increases with respect to both axisymmetric and non-axisymmetric disturbances for all values of L, and the stability boundaries shift to the right, corresponding to larger values of the Deborah number.

5.4. *Comparison of Chilcott–Rallison model stability calculations with experimental observations*

In order to compare our experimental observations with linear stability calculations it is first necessary to choose an appropriate value of the dumbbell extensibility L. As we have discussed above in §2.2 this parameter is best ascertained from extensional viscosity measurements; however, in the absence of such data we resort to fitting the shear-rate dependence of the first normal stress coefficient $\Psi_1(\dot{\gamma})$ for the 0.31 wt% PIB Boger fluid. Nonlinear regression results in the best fit value of $L \approx 15$ given in table 1. However, calculations with such a small value of L result in growth of spiral instabilities only at very large values of De_0 (cf. figure 17). Recent birefringence measurements in extensional flows through packed beds (Evans, Shaqfeh & Frattini 1994) suggest that the molecular extensibility of the PIB molecules in a Boger fluid is actually considerably larger than the value obtained from only considering the weak shear-rate-dependent variations in the viscometric properties, and values in the range $30 \leqslant L \leqslant 100$ are typically obtained for the extensibility of the dumbbells in the Chilcott–Rallison constitutive model. In the comparison presented below, we find numerical stability calculations with values of $L = 30$ and $L = 50$ best describe the experimentally measured critical conditions for the 0.31 wt% PIB and 0.20 wt% PIB fluid respectively. This discrepancy between experimental and numerical values of the nonlinear parameter L is to be expected considering the limitations inherent in describing a polydisperse semidilute polymer solution with a single-mode FENE dumbbell model. A more accurate comparison of experimental observations with linear stability analysis for a multimode nonlinear viscoelastic constitutive equation has recently been presented by Öztekin, Brown & McKinley (1994).

A composite stability diagram for comparison of experimental observations and numerical calculations of the cone-and-plate instability in each fluid can be constructed in several ways. The numerically determined critical cone angles for the most unstable azimuthal mode can be plotted as a function of the Deborah number De_0, as we have shown earlier in figure 18. However for consistency with the earlier work of McKinley *et al.* (1991), and our previous comparison with the Oldroyd-B model (cf. figure 15) we choose to present the stability diagram here in terms of the critical Weissenberg number $We_{crit} \equiv \lambda_1 \Omega / \theta_{0crit}(\alpha_{\xi crit}, m_{crit})$ as a function of the zero-shear-rate Deborah

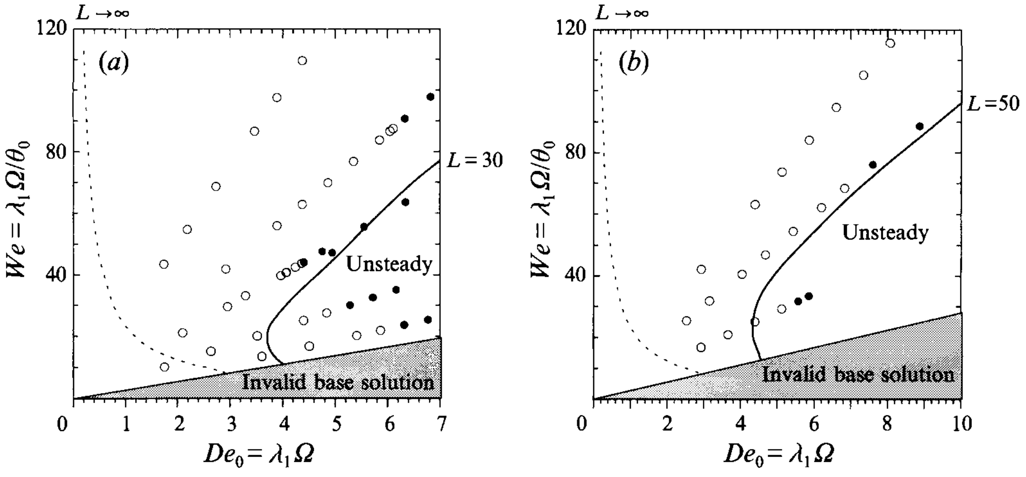

FIGURE 19. Comparison of experimentally determined and numerically calculated stability diagrams for onset of spiral instabilities between a cone and a plate in Boger fluids with solvent viscosity ratios of (*a*) $\beta = 0.59$ and (*b*) $\beta = 0.84$. In each figure symbols indicate experimental measurements of steady (○) or unsteady (●) base flow, dashed lines indicate predictions of the Oldroyd-B model with appropriate value of β, and solid lines indicate predictions of the Chilcott–Rallison model with indicated value of L.

number De_0, for the appropriate values of the solvent viscosity ratio, $\beta = 0.59$ and $\beta = 0.84$ respectively. In this parameter space, sets of experimental data points with a given conical fixture thus describe straight lines extending from the origin with slope $1/\theta_0$. Experimental measurements in each fluid corresponding to stable and unstable base flow are marked in figure 19 by open and closed circles, respectively. For comparison, the predictions from the linear stability analysis for the most dangerous azimuthal disturbances are also shown in figure 19 for both the Oldroyd-B limit ($L \to \infty$) and for the nonlinear Chilcott–Rallison model with a value of L that best fits the experimental data.

In contrast to the comparison presented previously in figure 15, there is no *ad hoc* adjustment in the relaxation time made here and each figure represents a direct comparison. The experiments in the 0.31 wt% PIB Boger fluid ($\beta = 0.59$) indicate that the critical Deborah number, below which no instability is seen, is $De_{0crit} \approx 4.25$ and also show that for small cone angles ($\theta_0 \leqslant 4°$) the base flow is stable for all values of rotation rate experimentally achievable in our experimental device. Also shown for completeness on this figure are additional experimental measurements performed earlier in a standard rheometer (McKinley 1991) using a conical fixture with $\theta_0 = 2.54°$ (0.04 rad). These observations are in sharp contrast to the predictions for the Oldroyd-B model, which is qualitatively incorrect and predicts $De_{0crit} \to 0$ for $We \gg 1$. The experimental observations and the linear stability calculations for the Chilcott–Rallison FENE dumbbell model with $L = 30$ and $\beta = 0.59$ are not in quantitative agreement; however, the general characteristics are correct. The predicted value of the critical Deborah number is $De_{0crit} \approx 3.75$ which is close to the value determined by experiments. The analysis also predicts that the viscometric flow is stable to all disturbances for all cone angles below about $\theta_0 \approx 4.7°$ (0.08 rad).

The stability diagram shown in figure 19(*b*) also provides an explanation for the initially puzzling observation discussed in §3.3 of a large increase in the critical Deborah number required for onset of instability in our experiments with the

0.20 wt% fluid in the 6° geometry. The increase in the solvent viscosity ratio, β, shifts the neutral stability curve for onset of spiral disturbances to higher Deborah numbers, and the locus of points in We–De_0 parameter space that are accessible with a 6° conical fixture now intersects the neutral stability curve in the region where shear-thinning effects in the normal stress result in increasing stabilization of the base azimuthal flow. A more extensive series of experiments with a large number of different conical fixtures would allow us to map out the experimental stability boundaries with even greater precision; however, it is clear that the nonlinear constitutive model is capable of describing the key features of the stability diagrams obtained in cone-and-plate experiments with Boger fluids.

6. Discussion

The overall pictures of the purely elastic spiral instability in a cone-and-plate rheometer observed by experiments and predicted by a linear stability analysis are in good agreement. Flow visualization experiments with two PIB/PB/C14 Boger fluids reveal the development of a secondary flow with the spatial form of logarithmic spirals that propagate radially inward across the gap. There is no preferred radial location at which this instability initially develops and spiral vortices are observed throughout the fluid sample. These video-imaging observations are consistent with the predictions of linear stability analyses for both the Oldroyd-B and Chilcott–Rallison constitutive models with appropriate choices of the solvent viscosity and dumbbell extensibility. For a range of cone angles and Deborah numbers, the homogeneous azimuthal shearing motion between the cone and plate is found to be unstable and the most linearly unstable modes have the form of logarithmic spiral vortices travelling either radially inward or outward. Disturbances of this form are found to be self-similar and independent of the radial coordinate $\hat{r}$, hence there is no particular radial location or region within which the disturbances are confined. Both the axisymmetric and non-axisymmetric spiral vortices are found to have very similar critical onset conditions for a solvent viscosity ratio of $\beta = 0.59$.

The spatial characteristics of the instability calculated with the Oldroyd-B model agree well with the experimental measurements (cf. figure 15). Both the video-imaging observations and the numerical calculations show that the radial spacing of the travelling spiral vortices becomes smaller for small values of the cone angle and that the azimuthal mode number increases. Stability analysis for both axisymmetric and non-axisymmetric disturbances shows a similar weak geometric variation of the critical wavenumber α_ξ for cone angles in the range of $6° \leqslant \theta_0 \leqslant 15°$. However, the predicted value of the critical wavenumbers of all disturbances sharply increases for smaller values of the cone angle $\theta_0 < 5°$; therefore, the winding number $n_{crit} \equiv -m/\alpha_{\xi crit}$ for the logarithmic spirals approaches zero as $\theta_0 \rightarrow 0°$. As a result, in this limit, the logarithmic spirals will closely resemble concentric axisymmetric waves. In order to observe the non-axisymmetric structure of the secondary flow, it is thus critical to observe the entire planform of the flow geometry.

The predictions of the temporal behaviour of the instabilities are also consistent with experiments, although the quantitative agreement is less satisfying than for the spatial characteristics. Experimental observations clearly show logarithmic spiral vortices that travel radially inward with a dimensionless wave speed of $-0.015 < c_\xi < -0.007$ for different values of the cone angle. The predicted values of wave speed for the axisymmetric and non-axisymmetric disturbances are indicated in figure 14(*b*) and vary between $-0.027 < c_\xi < -0.008$ for the range of cone angles $6° \leqslant \theta_0 \leqslant 15°$. As the cone angle approaches zero, the wave speeds for each azimuthal mode also approach zero and the disturbances become almost stationary.

The stability boundaries for purely azimuthal motion in a cone-and-plate rheometer that have been determined experimentally with highly elastic constant-viscosity fluids in a number of previous investigations can be accurately predicted using this Oldroyd-B linear stability analysis only if the single relaxation time constant λ_1 in this quasi-linear model is adjusted to include the shear-rate dependence of the first normal stress coefficient actually observed in the experimental test fluids. However, the stability predictions obtained using the quasi-linear Oldroyd-B constitutive model do not capture all features of this elastic instability. Experiments show that there is a range of cone angles for which no elastic instability is observed. Even with the *ad hoc* incorporation of shear thinning via an 'apparent relaxation time' $\lambda_1(\dot{\gamma})$, the analysis for the Oldroyd-B fluid model predicts onset of instability for small enough cone angles at all non-zero values of the Deborah number. To describe such observations, a more realistic constitutive model is required in which shear-thinning viscometric phenomena are incorporated implicitly via more detailed consideration of the macromolecular conformations in polymer solutions (Rallison & Hinch 1988).

A linear stability analysis for the Chilcott–Rallison model provides a more detailed description of this elastic spiral instability. Incorporating finite extensibility of the polymer chains does not appreciably modify the spatial and temporal characteristics of the disturbance at onset of the elastic instability, but it does change the stability boundaries for the base flow. Calculations with an extensibility parameter of $L = 30$ predict a non-zero value of the critical Deborah number (below which spiral instabilities are not observed for any cone angle) that is reasonably close to the measured value of $De_{0crit} \approx 4.25$. The shape of the stability boundary predicted by the Chilcott–Rallison model is also qualitatively in agreement with the experimental data (cf. figure 19) without resort to *a posteriori* adjustment of the fluid viscometric properties; however, the quantitative comparison is still not perfect. The values of the FENE dumbbell extensibility parameters ($L = 30$ or 50) used in our comparisons for the 0.31 wt% and 0.20 wt% PIB Boger fluids respectively, were selected to provide the most reasonable description of the experimental stability data over the range of parameter space represented in figure 19. Such values agree well with estimates that can be deduced from recent uniaxial elongation studies with the 0.31 wt% PIB Boger fluid performed by Tirtaatmadja & Sridhar (1993). However, these values are *inconsistent* with the much smaller values of $L = 15$ or 20 independently obtained from regression to our steady shear flow rheological data. The most plausible explanation for this discrepancy lies in the poor approximation of the single-mode constitutive models to the linear viscoelastic spectrum of the test fluids. Previous rheological studies of the viscometric properties of these Boger fluids clearly indicate a spectrum of relaxation times (Quinzani *et al.* 1990). Even in experiments with monodisperse polymer solutions, a larger number of relaxation modes are available for microscopic deformation of the polymer chains and different macroscopic viscometric tests probe differently weighted averages of this relaxation spectrum (Larson *et al.* 1994). It should not be expected that a simple single-mode FENE dumbbell model can capture such phenomena even qualitatively. A detailed stability analysis with a multimode constitutive model might improve the quantitative comparison between theory and experiments, particularly since earlier rheological studies indicate that different nonlinear coefficients (e.g. FENE extensibilities) are associated with different deformation modes (Quinzani *et al.* 1990). This possibility has been investigated by considering the stability of torsional motion between a cone and a plate with 4-mode formulations of the Oldroyd-B and Giesekus models. The results of this comparison are described by Öztekin *et al.* (1994) and show excellent agreement between analysis and experiment.

In the earlier work of Phan-Thien (1985), incorporation of shear-rate-dependent material functions via the Phan-Thien–Tanner nonlinear network model was found to entirely eliminate a purely elastic cone-and-plate instability of von Kármán form that had been found for the Oldroyd-B model. The logarithmic spiral instability documented in the present work persists even when nonlinear fluid rheology is incorporated and thus appears to be inherent to cone-and-plate flows of many viscoelastic fluids. Indeed the spatio-temporal characteristics of this instability, i.e. spiral recirculating vortices that translate spatially at speeds much slower than the rotation rate of the cone, are consistent with the very early observations of Kocherov *et al.* (1973) in polymer melts and of Kulicke & Porter (1979) in shear-thinning concentrated polymer solutions. Very recent observations in our device with a shear-thinning PIB/PB/Decalin solution (the 'S1' international test fluid) have confirmed the onset of a spiral flow instability in this fluid; however, the shear-rate-dependent material functions appear to amplify the nonlinear spatial mode interactions and the weak spiral secondary flow rapidly evolves into the fully nonlinear state characterized by figure 3(*d*).

The analyses for both constitutive models predict that the differences in the critical onset conditions between the axisymmetric and the most dangerous azimuthal modes are very small (see, for example, figure 14); hence it might be difficult to distinguish between these modes in the experiments. In fact, in the nonlinear stage of the flow visualization experiments, several modes including inward- and outward-winding spirals and the axisymmetric vortices are observed simultaneously. The precise ordering of the modes is also found to be a sensitive function of the solvent viscosity ratio and axisymmetric modes are predicted to be most unstable for values of $\beta > 0.6$. Recent observations of the cone-and-plate instability in a polystyrene-based Boger fluid appear to confirm the existence of axisymmetric disturbance modes (S. J. Muller 1993, personal communication).

The azimuthal modes predicted by the analysis are in the form of Archimedean spirals in the (ξ, θ, ϕ)-transformed domain, and hence are similar to the non-axisymmetric disturbances predicted by BÖBM for viscoelastic torsional flow between coaxial parallel rotating disks. However in the $(\tilde{r}, \theta, \phi)$ physical coordinate system of the cone-and-plate geometry these azimuthal modes represent logarithmically spaced Bernoulli spiral vortices. Although the number of logarithmic spirals predicted by the experiments and stability analysis for the Boger fluid with $\beta = 0.59$ is not exactly the same, the critical winding numbers n_{crit} are in close agreement. For a cone angle of $\theta_0 = 10°$ and a fluid with $\beta = 0.59$, only a single logarithmically spaced spiral vortex is observed in the experiments, while a linear stability analysis predicts the $m = \pm 2$ spiral modes to be the most unstable disturbances. The critical value of the expansion coefficient n_{crit} is measured to be 0.047 and is calculated to be 0.046. This discrepancy in the prediction of the number of spiral vortices may be resolved by studying multimode models, incorporating the finite nature of the cone-and-plate rheometer, or by considering the evolution of the amplitude of the individual travelling disturbance modes at Deborah numbers above the neutrally stable conditions. This latter consideration requires weakly and/or fully nonlinear stability analysis of the three-dimensional time-dependent spiral disturbances. Similar analyses that are just beginning for elastic instabilities in the Taylor–Dean and Taylor–Couette systems

(Shaqfeh 1993; Sureshkumar, Beris & Avgousti 1994) suggest that both the temporal frequency and ordering of unstable modes are modified by nonlinear interactions.

In our experiments very near the critical conditions for onset of the cone-and-plate instability we have always observed negative-angle ($m < 0$) non-axisymmetric logarithmic spiral modes. Conversely, in the parallel-plate geometry our experimental observations near the critical conditions have always revealed positive-angle ($m \geqslant 0$) spiral modes. The linear analysis presented in this work and in BÖBM, however, indicates that in each case both the positive-angle ($m > 0$) and negative-angle ($m < 0$) spiral modes are equally unstable. Presumably, this symmetric ordering of the $m = \pm M$ modes is destroyed by consideration of nonlinear interactions in finite-amplitude disturbances. In the absence of a nonlinear amplitude analysis it is difficult to satisfactorily explain the differences between the dynamics of the two elastic instabilities; however, we speculate that it may arise from the kinematic differences between the base-state azimuthal motions that we have considered in each geometry and from imperfections to these idealized one-dimensional base flows.

In the cone-and-plate geometry, the base state motion (in the limits $De_0 \ll 1$, $Re \ll 1$, and $\theta_0 \ll 1$) is a homogeneous azimuthal flow only to leading order. The resulting tensile elastic hoop stress coupled with the curvature of the closed circular streamlines drives a steady weak secondary recirculation superposed on this azimuthal motion that is *inwardly* directed near the rotating cone with magnitude $O(De_0 \theta_0)^2$. This elastic stress-driven steady secondary flow is not incorporated in our analysis and may lead to the negative or inward motion of the unsteady secondary flow that develops throughout the fluid sample after onset of instability. By contrast, for creeping motion between coaxial parallel plates, the base solution of purely azimuthal shear flow is exact. However, the flow is non-homogeneous and the elastic stresses vary in the radial direction. This results in a critical radius R_1^* below which all disturbances are damped out. Inward-travelling modes excited at this radial location will therefore translate to smaller radii and immediately decay; it is therefore not surprising that the finite-amplitude unstable modes observed experimentally are positive-angle, outward-travelling Archimedean spirals.

Our experimental observations in the cone-and-plate rheometer show that the outward-winding or negative angle ($m < 0$) logarithmic spirals travel radially *inward* and that the wave speed of the spiral vortices scales linearly with the radius $\hat{r}$ as described by equation (8). The sign of the imaginary part of the growth rate $\mathrm{Im}(\sigma)$ independently determined from the stability analysis also predicts that negative-angle spirals travel radially inwards (i.e. $c_\xi < 0$). Interestingly, the axisymmetric ($m = 0$) disturbance also is found to be an inward-travelling mode in the cone-and-plate geometry. By contrast, our analysis for the parallel-plate geometry predicted that the axisymmetric mode travels radially outwards.

Throughout this work we have emphasized that the spatial structures of the elastic instabilities presented in this paper for the viscoelastic flow between a cone and a plate are very different from those predicted by Öztekin & Brown (1993) and BÖBM for the flow between coaxial parallel rotating disks. However, the numerous similarities between the base torsional motion in two geometries and the form of the disturbance equations (after coordinate transformation in the cone-and-plate or radial localization in the parallel-plate configuration) suggest that these two spiral instabilities should be closely related. In the limit $\theta_0 \to 0°$, the radial variation in the local gap between the cone and the plate $h(\hat{r}) = \hat{r}\theta_0$ is very weak. If we consider localized displacements $\delta\hat{r}$ about an arbitrary radial position such as R_0 then we can linearize the logarithmic radial coordinate transformation (equation (2)) as $\xi = \ln(1 + \delta\hat{r}/R_0) \approx \delta\hat{r}/R_0$. Sub-

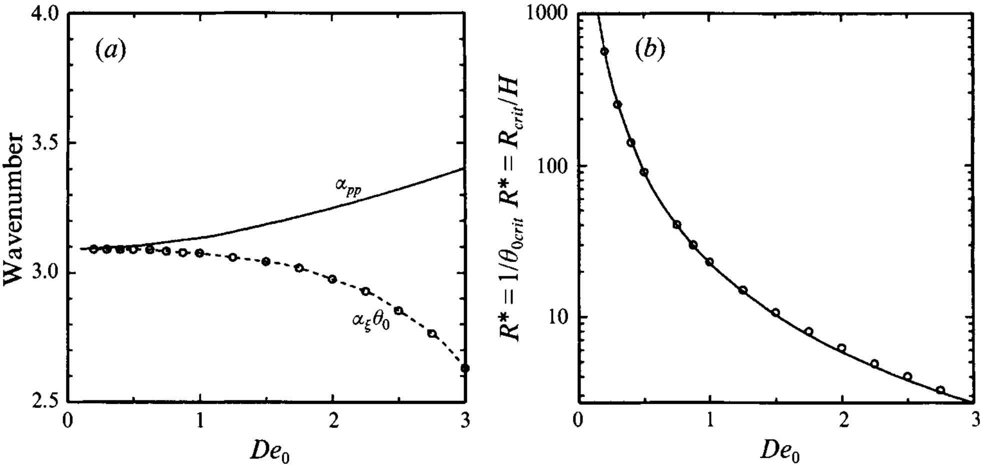

FIGURE 20. Connection between elastic instabilities in torsional motion between parallel rotating disks (Öztekin & Brown 1993) and between a cone and a plate. (*a*) The critical wavenumber (α_{PP}) of axisymmetric disturbances in the parallel plate (——), and the critical modified wavenumber $\alpha_\xi \theta_0$ in the cone and plate (---). (*b*) The critical geometric parameter R^*_{crit} for onset of axisymmetric disturbances in each geometry; ——, parallel plate; ○, cone and plate. All calculations are for the Oldroyd-B model with $\beta = 0.59$.

stituting this linearized transform coordinate into the disturbance kinematics described by (3), and defining the local gap between the two fixtures as $R_0 \theta_0 \equiv H$, leads to

$$\exp[\mathrm{i}\alpha_\xi \xi + \mathrm{i}m\phi + \sigma t] \approx \exp[\mathrm{i}(\alpha_\xi \theta_0)(\delta\hat{r}/H) + \mathrm{i}m\phi + \sigma t]. \tag{28}$$

By identifying the modified spatial wavenumber appearing in (28) as $\alpha_\xi \theta_0 \equiv \alpha_{PP}$, it becomes clear that this normal mode decomposition is equivalent to the form of the Archimedean spiral disturbances considered in BÖBM. In the limit of small cone angles (i.e. $R^* \equiv 1/\theta_0 \rightarrow \infty$) we expect the dimensionless product $\alpha_\xi \theta_0$ constructed from the spatial wavenumber of the cone-and-plate disturbance to approach the dimensionless radial wavenumber α_{PP} of the parallel-plate disturbance that can be obtained in the limit $R^* \equiv R/H \rightarrow \infty$ by linearizing the radial variations in the corresponding disturbance equations (Öztekin & Brown 1993). To verify this interconnection between the two elastic instabilities, we show in figure 20(*a*) the appropriate critical wavenumbers for the onset of axisymmetric instabilities in each geometry as a function of Deborah number for the Oldroyd-B model with $\beta = 0.59$. For this quasi-linear model the critical value of the geometric parameter R^* in each geometry becomes infinite in the limit as $De_0 \rightarrow 0$. Our calculations clearly show that although the dimensionless wavenumber α_ξ of the cone-and-plate disturbance becomes very large for small cone angles (cf. figure 14) the product $\alpha_\xi \theta_0$ approaches the same asymptotic value (≈ 3.1) as the wavenumber α_{PP} calculated for the parallel-plate disturbance in the limit $De_0 \rightarrow 0$. A similar comparison could be drawn from the predictions of the Chilcott–Rallison model; however, for each geometric configuration the curves would terminate at a non-zero value of the Deborah number, corresponding to the appropriate value of De_{0crit} below which all disturbances of spiral form are restabilized by shear thinning in the viscoelastic hoop stress.

Another connection between the linear stability predictions for the onset of elastic spiral instabilities in parallel-plate and cone-and-plate motions may be made by comparing the stability diagrams for the two geometries. The critical onset conditions for the axisymmetric disturbance modes for each geometry are plotted in figure 20(*b*) in terms of the appropriate critical geometric parameter, i.e. the critical radial location $R^* = \hat{r}_{crit}/H$ in the parallel-plate geometry and the critical cone angle $R^* = 1/\theta_{0crit}$ for the cone-and-plate geometry. Given the results in figure 20(*a*), it is not surprising that the predictions of R^* for both geometries are similar to one part in 1000 as $De_0 \rightarrow 0$. However, it is very interesting that the values of R^* remain very close for Deborah numbers as large as $De_0 = 3$. These results serve to justify two critical approximations made in the cone-and-plate and parallel-plate analyses. One is the approximation applied to find the solution of viscometric base flow between a cone and a plate. The results shown here indicate that the onset of instability is not particularly sensitive to the approximate form of the solution for the purely azimuthal base flow. At $De_0 = 3$ the critical cone angle becomes as large as 15°–20°; however, the corresponding value of $R^* \equiv 1/\theta_0 \approx 3$ remains close to the value of $R^* \equiv \hat{r}_{crit}/H$ for flow between parallel plates, in which the kinematics of the inertialess base flow are exact. Secondly, figure 20(*b*) shows that the critical conditions for onset of spiral instabilities in the parallel-plate configuration are insensitive to the approximation of localizing the disturbances. As we have described in section §4, disturbances in the cone-and-plate geometry are not localized to any particular region, in contrast with our earlier analysis for flow between parallel plates. The very close agreement in the values of the critical geometric parameters R^* for the onset of both instabilities over a wide range of Deborah numbers serves to justify the localized disturbance assumption first applied by Öztekin & Brown (1993).

Although the form of the instabilities is different in the cone-and-plate and parallel-plate geometries, the spatial structure of the disturbance velocities and the nature of the neutral stability diagrams are very similar. Hence, we expect that the physical mechanism responsible for the instabilities in both cases also is similar. The common feature of the viscoelastic instabilities now extensively documented for Taylor–Couette and Taylor–Dean flows, for torsional motion between parallel coaxial rotating disks, and for flow in a cone-and-plate rheometer is the coupling between the streamline curvature and the elastic normal stresses in the fluid. A detailed energy analysis and micromechanical discussion of the instability mechanism for axisymmetric and non-axisymmetric disturbances in the Taylor–Couette flow of an Oldroyd-B fluid has been given by Joo & Shaqfeh (1992, 1994) and a similar energy analysis for the nonlinear Chilcott–Rallison model was first given in BÖBM. We therefore do not repeat such calculations in detail here; however, the physical mechanisms associated with onset of the instability can be simply understood by considering interactions between infinitesimal fluctuations in the velocity gradient in the θ-direction and the base-state polymeric stresses which couple through the curved streamlines of the base flow to create a perturbation in the hoop stress $S_{\phi\phi}$ that reinforces the secondary flow.

For simplicity we consider an axisymmetric disturbance velocity field which results in a non-zero meridional velocity gradient $\partial u_\theta/\partial\theta$ that stretches the dumbbell in the θ-direction. Such disturbances create a perturbation to the meridional normal stress component $S_{\theta\theta}$ which satisfies

$$\mathrm{H}(S_{\theta\theta}) = 2\beta_p\, \partial u_\theta/\partial\theta, \tag{29}$$

where H( ) is the operator defined in 20(*g*).

The velocity gradient $\partial u_{0\phi}/\partial\theta$ and shear stress $S_{0\phi\theta}$ of the steady base flow couple with the meridional disturbances in $S_{\theta\theta}$ and $\partial u_\theta/\partial\theta$ to produce a perturbation in the shear stress given by

$$\mathrm{H}(S_{\theta\phi}) = De\, S_{\theta\theta}\frac{\partial u_{0\phi}}{\partial\theta} + De\, S_{0\theta\phi}\,\partial u_\theta/\partial\theta. \tag{30}$$

Additional coupling between this perturbation to the shear stress $S_{\theta\phi}$ and the base-state velocity gradient $\partial u_{0\phi}/\partial\theta$ further deforms the dumbbell in the azimuthal ϕ-direction which produces an additional hoop stress $S_{\phi\phi}$:

$$\mathrm{H}(S_{\phi\phi}) = 2De\, S_{\theta\phi}\, \partial u_{0\phi}/\partial\theta. \tag{31}$$

This additional elastic hoop stress reinforces the velocity field of the perturbation because of the curvature of the streamlines. The dominant terms in the transformed ξ- and θ-momentum equations, (19), for the disturbance motion are independent of radial position and given by

$$-S_{\phi\phi} - \partial p/\partial\xi + \beta\nabla^2 u_r = 0, \quad -\partial p/\partial\theta + \beta\nabla^2 u_\theta = 0. \tag{32a, b}$$

The disturbance path followed here is very similar to that of the parallel-plate case and computations of the mechanical energy balance for this creeping flow are analogous to those discussed by Joo & Shaqfeh (1994) for the viscoelastic Taylor–Dean instability. Such calculations show similar couplings between the steady base flow and the disturbances, plus the presence of an additional damping term arising from the finite extensibility of the dumbbells which, in this geometry, is independent of radial position but becomes increasingly important at higher shear rates. The only unique features in the cone-and-plate geometry are the lack of radial variation in the rate of disturbance energy production and the absence of terms in the energy balance equations involving *gradients* of the elastic stress field resulting from the purely azimuthal base flow because this motion is spatially homogeneous, unlike Taylor–Dean flow or torsional motion between parallel plates.

The results presented in this paper have clearly shown that the elastic flow instabilities responsible for apparent anti-thixotropic transitions observed in cone-and-plate rheometers are similar to those in the parallel-plate rheometer. These flow instabilities have very important consequences in correctly interpreting rheological measurements performed in highly elastic liquids. For a given cone angle, the disturbances take the form of travelling logarithmic spiral vortices and render the azimuthal steady-state viscometric motion unstable beyond a critical value of the Deborah number. These elastic instabilities occur even in creeping flows using conical fixtures with cone angles as small as $\theta_0 \approx 4°$ which are commonly employed in commercial rheometers. The restabilization of the base flow at higher shear rates (or equivalently smaller cone angles) suggests that even shallower cones should be used to avoid erroneous viscometric measurements.

G.H.M. would like to thank The Merck Trust and the NSF Research Initiation Award Program for the support of this research. The efforts of the other authors were supported by the Fluid Mechanics and Hydraulics Program of the NSF.

REFERENCES

Bird, R. B., Armstrong, R. C. & Hassager, O. 1987*a* *Dynamics of Polymeric Liquids. Volume 1: Fluid Mechanics*, 2nd Edn, Wiley Interscience.

Bird, R. B., Curtiss, C. F., Armstrong, R. C. & Hassager, O. 1987*b* *Dynamics of Polymeric Liquids. Volume 2: Kinetic Theory*, 2nd Edn, Wiley Interscience.

Bird, R. B., Stewart, E. S. & Lightfoot, E. N. 1960 *Transport Phenomena*. Wiley Interscience.

Boger, D. V. 1977/78 A highly elastic constant-viscosity fluid. *J. Non-Newtonian Fluid Mech.* **3**, 87–91.

Byars, J. A., Öztekin, A., Brown, R. A. & McKinley, G. H. 1994 Spiral instabilities in the flow of highly elastic fluids between rotating parallel disks. *J. Fluid Mech.* **271**, 173–218.

Chilcott, M. D. & Rallison, J. M. 1988 Creeping flow of dilute polymer solutions past cylinders and spheres. *J. Non-Newtonian Fluid Mech.* **29**, 381–432.

Evans, A. R., Shaqfeh, E. S. G. & Frattini, P. L. 1994 Observations of polymer conformation during flow through a fixed fibre bed. *J. Fluid Mech.* **281**, 319–356.

Giesekus, H. 1963 Some secondary flow phenomena in general viscoelastic fluids. In *Proc. 4th Intl Congr. Rheology, Brown Univ.*, Vol. 1, pp. 249–266. Wiley.

Griffiths, D. F. & Walters, K. 1970 On edge effects in rheometry. *J. Fluid Mech.* **42**, 379–399.

Heuser, G. & Krause, E. 1979 The flow field of Newtonian fluids in cone-and-plate rheometers with small gap angles. *Rheol. Acta* **18**, 531–564.

Hudson, N. E. & Ferguson, J. 1990 The shear flow properties of M1. *J. Non-Newtonian Fluid Mech.* **35**, 159–168.

Joo, Y. L. & Shaqfeh, E. S. G. 1992 The effects of inertia on the viscoelastic Dean and Taylor–Couette flow instabilities with application to coating flows. *Phys. Fluids* A **4**, 2415–2431.

Joo, Y. L. & Shaqfeh, E. S. G. 1994 Observations of purely elastic instabilities in the Taylor–Dean flow of a Boger fluid. *J. Fluid Mech.* **262**, 27–73.

Kocherov, V. L., Lukach, Y. L., Sporyagin, E. A. & Vinogradov, G. V. 1973 Flow of polymer melts in a disc-type extruder and in rotational devices of the 'cone-plate' and 'plate-plate' type. *Polymer Engng Sci.* **13**, 194–201.

Kulicke, W. M. & Porter, R. S. 1979 Irregularities in steady flow for non-Newtonian fluids between cone and plate. *J. Appl. Polymer Sci.* **23**, 953–965.

Larson, R. G. 1992 Instabilities in viscoelastic flows. *Rheol. Acta* **31**, 213–263.

Larson, R. G., Muller, S. J. & Shaqfeh, E. S. G. 1994 The effect of fluid rheology on the elastic Taylor–Couette flow instability. *J. Non-Newtonian Fluid Mech.* **51**, 195–225.

Laun, H. M. & Hingmann, R. 1990 Rheological characterization of the fluid M1 and of its components. *J. Non-Newtonian Fluid Mech.* **35**, 137–157.

Magda, J. J. & Larson, R. G. 1988 A transition occurring in ideal elastic liquids during shear flow. *J. Non-Newtonian Fluid Mech.* **30**, 1–19.

McKinley, G. H. 1991 The nonlinear dynamics of viscoelastic flow in complex geometries, PhD thesis, MIT.

McKinley, G. H., Byars, J. A., Brown, R. A. & Armstrong, R. C. 1991 Observations on the elastic instability in cone-and-plate and parallel-plate flows of a polyisobutylene Boger fluid. *J. Non-Newtonian Fluid Mech.* **40**, 201–229.

Olagunju, D. O. 1993 Asymptotic analysis of the finite cone-and-plate flow of a non-Newtonian fluid. *J. Non-Newtonian Fluid Mech.* **50**, 289–305.

Olagunju, D. O. & Cook, L. P. 1992 Secondary flows in cone and plate flow of an Oldroyd-B fluid. *J. Non-Newtonian Fluid Mech.* **46**, 29–47.

Olagunju, D. O. & Cook, L. P. 1993 Linear stability analysis of cone-and-plate flow of an Oldroyd-B fluid. *J. Non-Newtonian Fluid Mech.* **47**, 93–105.

Öztekin, A. & Brown, R. A. 1993 Instability of a viscoelastic fluid between rotating parallel disks: analysis for the Oldroyd-B fluid. *J. Fluid Mech.* **255**, 473–502.

Öztekin, A., Brown, R. A. & McKinley, G. H. 1994 Quantitative prediction of the viscoelastic instability in cone-and-plate flow of a Boger fluid using a multi-mode Giesekus model. *J. Non-Newtonian Fluid Mech.* **54**, 351–379.

Peitgen, H.-O., Jürgens, H. & Saupe, D. 1992 *Chaos and Fractals.* Springer.

Phan-Thien, N. 1985 Cone and plate flow of the Oldroyd-B fluid is unstable. *J. Non-Newtonian Fluid Mech.* **17**, 37–44.

Quinzani, L. M., McKinley, G. H., Brown, R. A. & Armstrong, R. C. 1990 Modeling the rheology of polyisobutylene solutions. *J. Rheol.* **34**, 705–748.

Rallison, J. M. & Hinch, E. J. 1988 Do we understand the physics in the constitutive equation? *J. Non-Newtonian Fluid Mech.* **29**, 37–55.

Sdougos, H. P., Bussolari, S. R. & Dewey, C. F. 1984 Secondary flow and turbulence in a cone-and-plate device. *J. Fluid Mech.* **138**, 379–404.

SHAQFEH, E. S. G. 1993 Weakly nonlinear analysis of the elastic Taylor–Couette instability. Presentation at the *VIIIth Intl Workshop on Num. Meth. in Viscoelastic Flows, Cape Cod, Oct. 21–24.*

STEIERT, P. & WOLFF, C. 1990 Rheological properties of a polyisobutylene in a kerosene/polybutene mixture in simple shear flow. *J. Non-Newtonian Fluid Mech.* **35**, 189–196.

SURESHKUMAR, R., BERIS, A. N. & AVGOUSTI, M. 1994 Non-axisymmetric subcritical bifurcations in viscoelastic Taylor–Couette flow. *Proc. R. Soc. Lond.* A (in press).

TIRTAATMADJA, V. & SRIDHAR, T. 1993 A filament stretching device for measurement of extensional viscosity. *J. Rheol.* **37**, 1081–1102.

TURIAN, R. M. 1972 Perturbation solution of the steady Newtonian flow in the cone-and-plate and parallel-plate systems. *Ind. Engng Chem. Fundam.* **11**, 361–368.

WALTERS, K. & WATERS, N. D. 1968 On the use of a rheogoniometer. Part I – Steady shear. In *Polymer Systems: Deformation and Flow* (ed. A. D. Wetton & A. Whorlow).